metals

MDPI

Article

Influence of Punch Shape on Joint Strength in Forge Joining of Al-Si-Coated 22MnB5 Steel During Hot Stamping and Application to Hat Bending

Jarupong Charoensuk [1], Takuma Iwai [2], Surasak Suranuntchai [1,3] and Tomoyoshi Maeno [2,*]

[1] Department of Tool and Materials Engineering, King Mongkut's University of Technology Thonburi, 126 Pracha Uthit Rd., Bang Mod, Thung Khru, Bangkok 10140, Thailand; jarupong.charo@mail.kmutt.ac.th (J.C.); surasak.sur@kmutt.ac.th (S.S.)
[2] Division of Systems Research, Faculty of Engineering, Yokohama National University, Yokohama 240-8501, Kanagawa, Japan
[3] Faculty of Engineering, Kasem Bundit University Rom Klao Campus, 60 Rom Klao Rd., Min Buri, Bangkok 10510, Thailand
* Correspondence: maeno-tomoyoshi-yf@ynu.ac.jp

Abstract

Ultra-high-strength steel sheets were joined by forge joining during hot stamping. This study investigated the influence of punch cross-sectional shape and punch tip inclination shape on joint strength through experiments and finite element simulation, with applications in hat bending. The experiments systematically evaluated various punch geometries by varying the punch's cross-sectional shape and the aspect ratio of rectangular punches. A second set of experiments focused on the influence of punch tip inclination shape. These experiments examined a rectangular punch with a slope. Joint strength is primarily assessed by measuring the tensile shear load. Finite element simulation was used to analyze joining mechanisms, investigating contact pressure and surface expansion rate distribution. The results from the experiments consistently indicated that, for a constant cross-sectional area, punch shapes with a larger punch perimeter on the upper sheet yielded a higher tensile shear load, though the changing inclination shape of the rectangular punch tip did not lead to an observed improvement in joint strength. Finite element simulation analysis revealed that punch shapes promoting a uniform distribution of contact pressure and surface expansion rate across the joint area tended to exhibit higher joint strength compared with the same punch cross-sectional area but less uniform distribution, a tendency that was more pronounced for the distribution of contact pressure than for the surface expansion rate.

Keywords: hot stamping; patchwork blanks; tailored blank; finite element simulation; hat bending; press hardening; solid state joining

Check for updates

Academic Editor: Zhengwei Li

Received: 25 February 2026
Revised: 19 March 2026
Accepted: 26 March 2026
Published: 28 March 2026

Copyright: © 2026 by the authors. Licensee MDPI, Basel, Switzerland. This article is an open access article distributed under the terms and conditions of the Creative Commons Attribution (CC BY) license.

1. Introduction

The critical demand to end global warming has put enormous pressure on the car industry to reduce CO_2 emissions. The transport industry, which is now the second largest carbon emitter globally, accounting for nearly a quarter of the world's carbon emissions, is a point of concern [1]. Therefore, reducing CO_2 from cars is crucial to combat climate change. One effective approach to this is reducing the vehicle weight, which directly improves fuel efficiency.

As fuel efficiency standards become increasingly stringent, the demand for advanced lightweighting technologies intensifies [2–4]. Body car frame components, typically

manufactured from high-tensile steel sheets ranging from 1 to 3 mm in thickness, constitute 30–40% of a vehicle's total weight. However, the requirements for increased collision safety led to increased car weights, which necessitate thicker plates and hence go against weight minimization. Therefore, the automobile industry is forced to develop innovative technologies that simultaneously minimize the vehicle weight, enhance driving safety, conserve energy, and minimize carbon dioxide emissions to satisfy both environmental demands and compliance requirements [3,5].

Manufacturing high-strength steel components presents significant challenges, particularly when using cold press forming. As tensile strength increases, steel sheet elongation decreases, leading to reduced workability and a higher risk of cracking. Additionally, higher tensile strengths accelerate cold press die wear. These factors, combined with increased forming loads, significant springback, and diminished formability, make cold press forming of high-tensile steel difficult and exceptionally challenging for ultra-high-tensile steel sheets exceeding 1.2 GPa. Consequently, hot stamping has become the widely adopted method for forming ultra-high-tensile steel, effectively overcoming these cold pressing drawbacks [6].

Hot stamping is a forming technique designed to produce high-strength components, particularly for automotive applications, offering significant weight reduction compared to traditional high-tensile steel sheets [3,7,8]. The process begins by heating quenchable steel sheets above their recrystallisation temperature, around 900 °C: the austenite phase. Subsequently, the heated sheet is transferred to a die for press forming. To achieve simultaneous forming and quenching, the member is held within the die, specifically at the bottom dead center, to facilitate heat removal. This die quenching step is crucial for attaining the desired high tensile strengths, often exceeding 1.5 GPa, in the final product, which is significantly higher than that of the cold-stamped parts [9]. In recent years, hot stamping has been widely used in automobiles to reduce weight and enhance crash safety [9,10]. A key advantage of hot stamping lies in its superior shape fixation, virtually eliminating springback and the capability of being formed in a single operation. These advantages enable the use of thinner materials, which in turn reduces the part weight and material costs, a common issue in cold press forming. In cold press forming, as the strength of the steel sheet increases, so does the forming load. This elevated load leads to greater elastic recovery upon unloading, resulting in significant springback. Conversely, hot-stamped materials exhibit minimal to no springback. This is attributed to the martensitic transformation, which is completed during the bottom dead center holding for die quenching. This transformation effectively minimizes the residual stress, which is the root cause of springback [11].

Automotive weight reduction employs both structural optimization and lightweight materials. Structurally, weight can be reduced without sacrificing strength by strategically varying the part thickness: it is thicker where strength is crucial and thinner elsewhere. This principle is realized through tailored blanks, which are integrated plate materials of differing thicknesses or materials [12,13]. Press-forming these blanks yields components with optimized plate thickness and strength distribution. For structural optimization in automotive components, both tailored and patchwork blanks are utilized. Tailored blanks, which can be further categorized into welded, rolled types, involve joining sheets with differing properties or thicknesses. Welded tailored blanks are commonly produced using laser welding and mash seam welding, and tailor-welded blanks offer advantages such as improved crashworthiness, structural stiffness, and formability [12]. Other methods like high-frequency, friction stir, electron beam, and induction welding are theoretically possible but less frequent. While welded tailored blanks contribute to automobile body weight reduction, they incur high investment costs for the welding process.

Patchwork blanks offer a key advantage over traditional tailor-welded blanks, by providing highly localized reinforcement in complex or internal areas of a component. While tailor-welded blanks are created by butt-welding sheets edge-to-edge to create a blank with different properties across its width, patchwork blanks use a lap-welded patch on top of a base blank. This allows for precise, targeted strength and thickness increases in small, specific zones, which is particularly beneficial for improving crashworthiness and stiffness without the significant material and weight additions that would be required to reinforce the entire part, a task that tailor-welded blanks are less suited for. Hot stamping patchwork blanks, in contrast to welded tailored blanks, which involve welding sheets together [14], utilize the overlapping patch materials' resistance that is spot-welded onto a base material for reinforcement [12,15,16]. A single patch can be spot-welded at multiple points, or multiple patches can be applied to a single base. This overlapping and spot-welding of patch materials precedes the heating and hot stamping stage. Unfortunately, this method introduces non-uniformity during heating, which negatively impacts the workability of the welded areas. An alternative to pre-heating patchwork blanks for joining is to integrate the joining process directly into hot stamping.

Resistance spot welding is typically used to join ultra-high-strength steel patchwork blanks [17]. Conventional hot stamping patchwork blanks present several limitations. The abundance of spot welds generates excessive stiffness, hindering formability during hot stamping and raising the likelihood of wrinkles and cracks [18,19]. The weld spots also disrupt the uniform material flow, resulting in relative sliding and the formation of defects during the forming process [14,16,19,20]. A critical factor for forming quality is achieving a homogeneous temperature distribution across a patchwork blank, especially at the weld, to avoid wrinkles and cracks. Materials with different thermal conductivities or thicknesses heat unevenly. A painting or coating technique can modify surface emissivity to control heating rates and improve temperature uniformity, but this process increases the manufacturing cost and time. Additionally, welding the patch components prior to heating leads to inconsistent temperature distribution, due to thickness differences. This uneven heating, particularly between overlapped and non-overlapped zones, causes variations in holding times at the plating temperature, potentially damaging the alloy layer in Al-Si plated materials [19].

Mori et al. [21] introduced a novel joining technique that relies on plastic deformation, offering a solution to the formability and weldability challenges encountered with conventional methods. Since it does not involve external heat like fusion welding, it avoids the related problems. This joining method is classified into metallurgical and mechanical processes. Instead of joining patchwork blanks before heating, a method of joining them simultaneously during hot stamping can be considered, with mechanical joining being one such approach. One promising mechanical joining technique is clinching, which uses plastic deformation with a simple punch and die to connect diverse sheet metals. This method contrasts with heat-intensive spot welding and offers several advantages, due to the absence of auxiliary components: reduced expenses, simplified setup, increased safety and environmental friendliness, reliable and robust joints, and extended durability [22,23]. However, achieving interlocking with high-strength, low-ductility lightweight materials like 22MnB5 can be challenging [24,25]. To overcome these challenges, Chen et al. [26] have developed an approach that integrates hot stamping technology into the clinching process. This method involves performing mechanical clinching while the material is being hot stamped. Mechanical clinching joins two plates by mechanically hooking them together without requiring additional parts, making it particularly suitable for automotive applications.

To overcome these limits, Abe et al. [27] resorted to severe interventions, utilizing a particle-laden adhesive to artificially amplify the friction and force material flow when

joining 980 MPa steel to aluminum. Finally, the joining characteristics of solid-state joining in hot stamping have not been clarified and need to be investigated. Mori et al. [19] developed a combined hot stamping and mechanical joining process for ultra-high-strength steel patchwork components. While the interlock successfully formed in the die step's space due to local buckling, laser welding was still necessary because the joint lacked sufficient strength.

Metallurgical joining methods represent another approach, such as cold and friction welding, which achieves bonding through intense plastic deformation. This process disrupts oxide layers and contaminants at the joining surfaces, and the resulting clean surfaces are forced together under high pressure. The internal heating caused by interfacial slippage and plastic work softens the materials, accelerating the bonding process. These methods, also known as solid-state welding [28], rely on significant plastic deformation to achieve a metallurgical bond.

Yamagishi et al. [29,30] recently introduced the cold spot forge-welding (CSFW) method as a high-productivity solution for achieving robust solid-state bonding. This technique was initially demonstrated through the successful joining of multiple aluminum (Al) foils to simulate the intricate structure of tab-lead electrodes. Building upon these findings, the approach was extended to achieve high-strength Cu/Al metallurgical joints. By utilizing instantaneous high-intensity pressure at low temperatures, the CSFW process strictly governs interfacial reactions, effectively suppressing the growth of brittle intermetallic compounds (IMCs) that typically plague conventional welding. This sequential development underscores the versatility of the CSFW method in producing high quality joints through precise solid-state interfacial control.

Producing ultra-high-strength steel (UHSS) patchwork blanks using conventional hot stamping presents significant challenges. Weld spots disrupt the uniform material flow, severely increasing the risk of wrinkles and cracks during forming. Alternatively, while traditional cold clinching offers a faster and more cost-effective solution, applying it to low-ductility UHSS is highly problematic. The material's susceptibility to fracturing and high flow stress require substantial punch loads, making the mechanical joining of steel grades exceeding 590 MPa profoundly difficult. To overcome these limitations, solid-state bonding has shown significant promise, albeit primarily for non-ferrous alloys. Its application to UHSS, specifically 22MnB5, remains completely unexplored. Crucially, there is a distinct lack of research investigating solid-state pressure welding under high-temperature hot stamping conditions. Furthermore, the systematic optimization of joining parameters for this elevated-temperature process has not yet been reported in the literature.

Therefore, this study introduces a combined hot stamping and metallurgical joining process, called forge joining, to minimize the need for auxiliary tools when joining ultra-high-strength steel sheets. This innovative technique achieves solid-state bonding of Al-Si-coated 22MnB5 steel during simultaneous hot stamping and joining. The primary objective of this study was to enhance the joining strength, which had been identified as a key challenge, and to determine the process parameters that contribute to its improvement. The research investigated the influence of the punch cross-sectional shape and slope angle on joint strength through a combination of experiments and finite element simulation. The simulations included a flow analysis aimed at examining the effects of contact pressure and surface expansion rate, which are both critical factors in pressure joining on the resulting joining strength.

2. Material and Methods

2.1. Forge Joining Method of Patchwork Blanks in a Hot Stamping Process

Conventional hot stamping of ultra-high-strength steel patchwork necessitates the initial joining of blanks by resistance spot welding, followed by furnace heating and subsequent hot forming, illustrated in Figure 1. A significant drawback of this approach is the potential for mechanical failure (rupture) at the resistance spot welds during hot stamping. This is because the poor workability of the welded area leads to a non-uniform stress state and increased resistance to the material flow, consequently raising the likelihood of plastic instability phenomena like wrinkling and cracking [18,19].

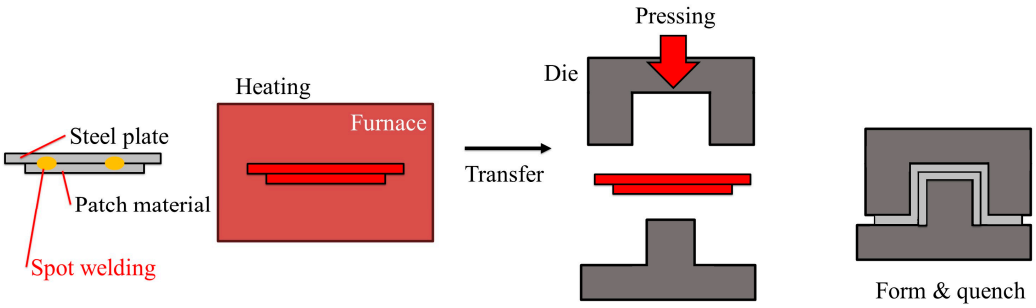


Figure 1. Conventional hot stamping process for patchwork blanks, integrated with resistance spot welding.

To mitigate the limitations of conventional methods, the forge joining process is implemented within a single hot stamping operation, with applications for hat bending in the hot stamping process of patchwork blanks. The experimental procedure for the joining process is illustrated in Figure 2. Additionally, Table 1 summarizes the chemical composition and the mechanical properties of the Al-Si-coated 22MnB5 ultra-high-strength steel sheets used in this study, which are determined through uniaxial tensile and hardness testing and are summarized in Table 2. First, two test specimens are stacked, spot-welded at the four corners for fixation, and then heated in a furnace (Koyo, Chiba, Japan) at 950 °C for 4 min. The heated specimens are then transported to the die and positioned correctly, using the locating pins. Then, the upper die is pressed and held at the bottom dead center for 10 s to perform both die quenching and joining. In forge joining, a technique that relies on plastic deformation to remove contaminants like oxides, bonding occurs quickly between nascent surfaces. This process, also known as solid-state bonding, reduces the interatomic distance to a stable state, allowing atoms to bond. At high temperatures, the active atoms on the bonding surfaces become highly mobile and diffuse into one another. As the atoms approach a distance where bonding forces can take hold, they form a solid-state bond. The increased ease of joining at high temperatures is due to the enhanced activity and familiarity of the atoms on the joining surfaces. Therefore, solid-state bonding requires heat to activate the atoms and plastic deformation to bring them into close contact for joining. Therefore, the forge joining process is highly suitable for hot stamping. To optimize the forge joining conditions, an experiment was conducted to investigate the phenomenon, as shown in Figure 3, under the same conditions as above.

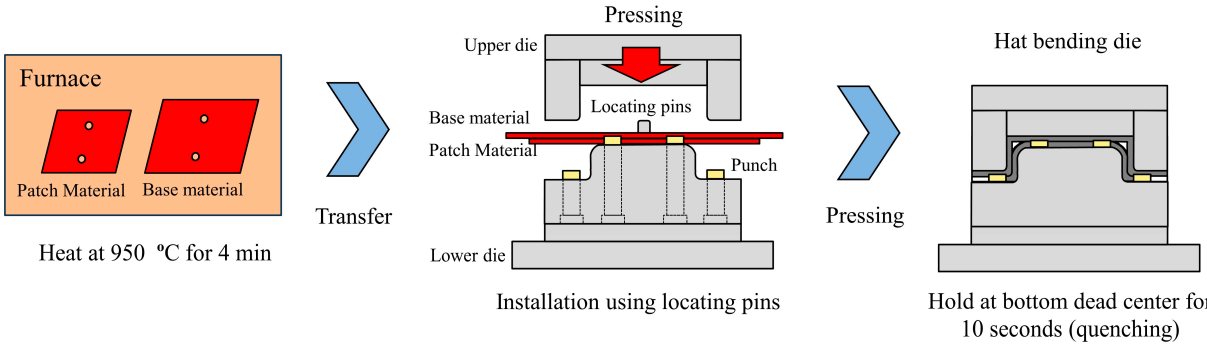


Figure 2. Hot stamping process of patchwork blanks, integrated with forge joining using a hat-shaped bending die.

Table 1. The chemical composition of 22MnB5 steel sheet.

Element	C	Si	Mn	P	B
Composition (mass%)	0.21	0.25	1.2	0.015	0.014

Table 2. The mechanical properties of die-quenched 22MnB5 steel sheet.

Tensile Strength	Thickness	Total Elongation	Vicker Hardness
1.53 GPa	1.6 mm	6.8%	480 VH1

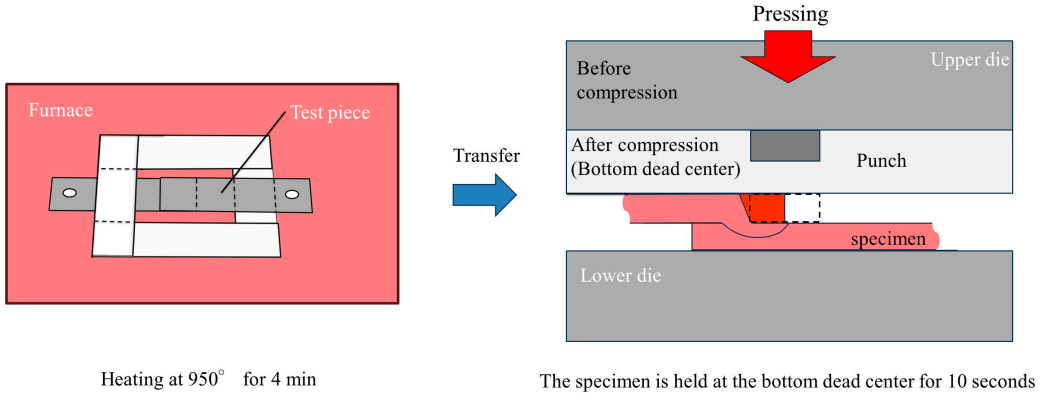


Figure 3. Experimental setup for the forge joining of a strip plate utilizing flat tools.

For ease of transport, the pieces are fixed during this heating period. After heating, specimens are transferred to a die in about 3 s. The dimensions of the die are shown in Figure 4. The die set conforms to the Japanese Industrial Standard (JIS) [31]. The die is attached to a die set, and the material of the die set is S50C (carbon steel). For the die, heat-treated SKS (alloy tool steel) material was used and S50C (carbon steel) was used for other parts. The process involves a protruding punch on the upper die surface, as shown in Figure 5a, which is aligned with the edge of the patch material. The punch was made from SKD11 (cold work tool steel). The lower die is flat, but a steel plate is attached to the lower die for positioning the specimen, as shown in Figure 5b. The overlapping parts of the strip plates are joined by compressing the edges with a flat die and a punch, making the joint portion easily deformable. This compression is performed using a press machine (Amada Machine Tools, Ltd., Kanagawa, Japan, electric servo press SDE-8018BO). For the investigation of the joining characteristics, forge joining experiments were specifically carried out on shim tape (thin stainless-steel sheet), as depicted schematically in Figure 6. The specimen had a thickness of 1.6 mm and a width of 20 mm. The nominal compression

ratio, s (%), is defined as the amount of upper die indentation at bottom dead center, relative to the total initial thickness of the steel plates. As illustrated in Figure 7 and Equation (1), this parameter represents the degree of vertical deformation imposed during the joining process.

$$s = \frac{h}{t_0} \times 100 \quad (1)$$

where s is the nominal compression ratio (%). h is the indentation depth of the upper die at the bottom dead center. t_0 is the initial total thickness of the steel plates.

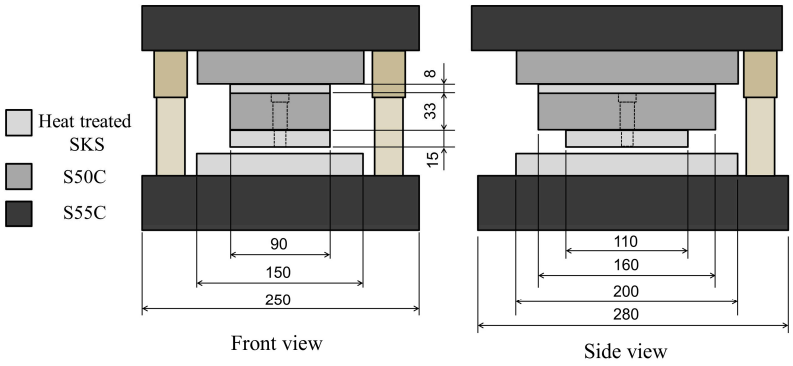


Figure 4. Dimensions of flat die for forge joining flat strip experiment [unit: mm].

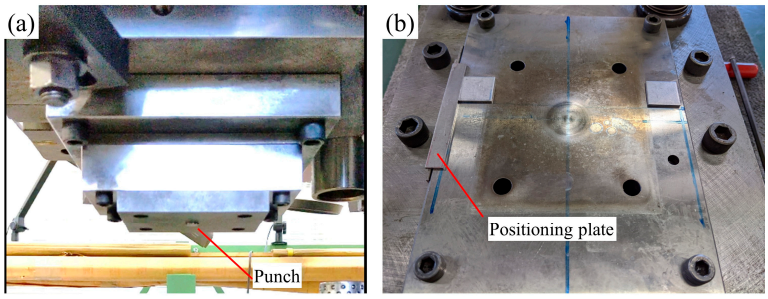


Figure 5. Flat die used in forge joining: (**a**) upper die and (**b**) lower die.

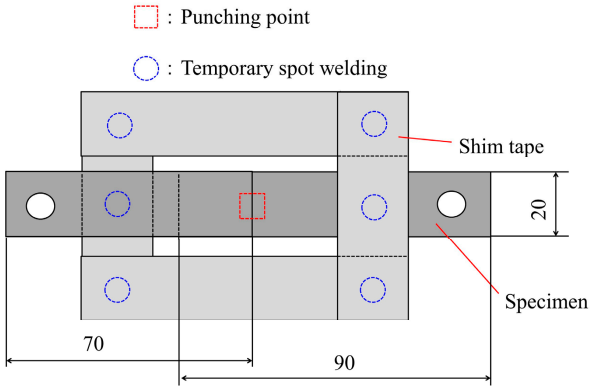


Figure 6. Dimensions of specimen and shim tape for forge joining flat strip experiment [unit: mm].

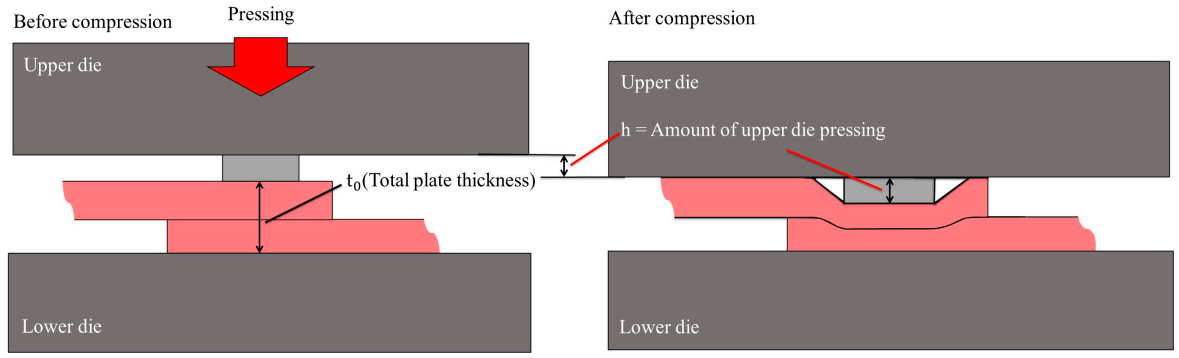


Figure 7. Schematic representation of the indentation depth and the derivation of the nominal compression ratio s at bottom dead center.

The various punch shapes employed are illustrated in Figure 8. An attempt was first made to find a stronger joint using circular and rectangular shapes and cross-shaped punches with the same projected area. Also, considering anisotropy, experiments were conducted with rectangular and cross-shaped punches rotated by 45° degrees. Furthermore, the effect of the aspect ratio of the punch projection surface on the joining strength was investigated. As shown in Figure 9, experiments were conducted using punches with the same projected area and aspect ratios (perpendicular to the tensile direction) of 1:2, 1:1, and 2:1, respectively. In addition to these changes in the punch shape in the longitudinal and plate width direction, to evaluate the effect of the punch tip inclination shape on the joint strength, three-dimensional changes were introduced to the punch shape in the plate thickness direction. As shown in Figure 10, the punch shape was changed in the plate thickness direction by providing an inclination to rectangular punches with the same cross-sectional shape at the punch tip.

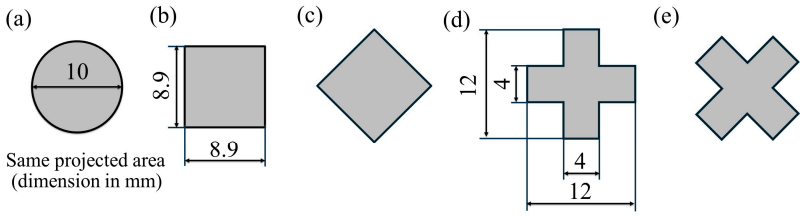


Figure 8. Punches with different cross-section shapes: (**a**) circle; (**b**) rectangle; (**c**) rectangle 45°; (**d**) cross; and (**e**) cross 45° [unit: mm].

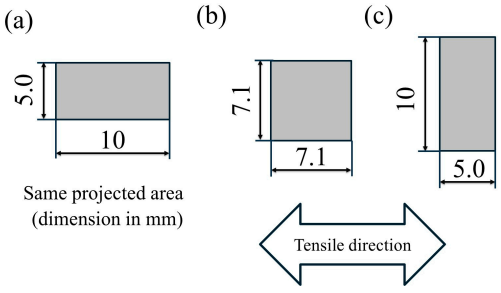


Figure 9. Rectangular punches with a projected area of 50 mm^2 and varying aspect ratios (width: longitudinal direction): (**a**) 1:2; (**b**) 1:1; and (**c**) 2:1 [unit: mm].

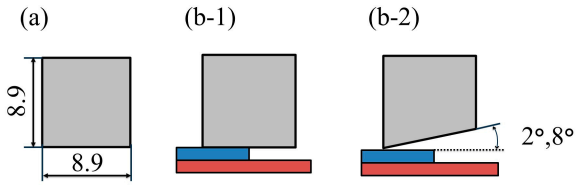


Figure 10. Punch tip: (**a**) cross-sectional view; (**b-1**) punches without inclination; and (**b-2**) punch with inclination [unit: mm].

2.2. Joint Strength Evaluation Method

A tensile shear test was conducted on the joined test pieces to evaluate the strength. Figure 11a shows the tensile shear test for the joined test pieces. As shown in Figure 11b, the test pieces were fixed with bolts instead of being directly gripped by the chuck and Figure 11c shows photographs of the tensile shear test. The tensile shear test was performed at a stroke speed of 5 mm/min. The measuring condition was chosen on the basis of the Japanese Industrial Standard Committee (JIS Z 3136) [32].

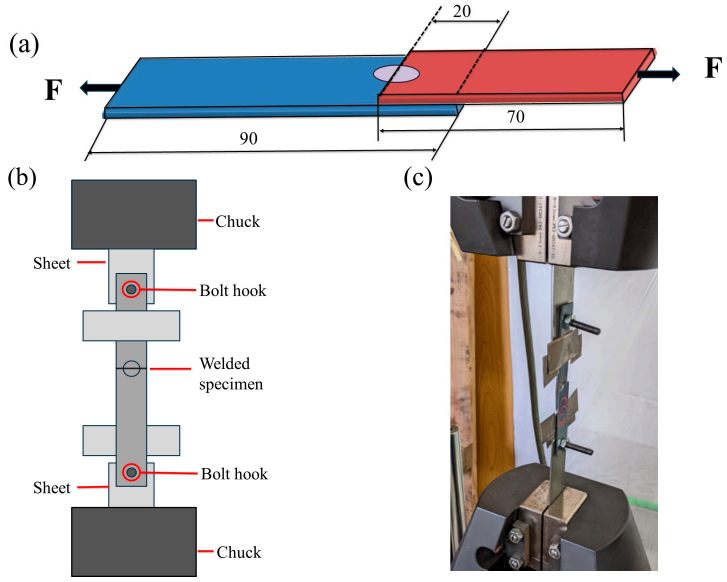


Figure 11. Tensile shear test in forge joining experiment: (**a**) tensile shear test red: upper plate, blue: lower plate; (**b**) schematic diagram; and (**c**) photograph.

2.3. Simulation Analysis Method for Forge Joining

A simulation analysis of the forge joining process was performed using Simufact Forming 2025, a commercial finite element software based on the nonlinear MSC Marc solver. The solution method employed a thermo-mechanical coupled analysis, using a static implicit method. The thermomechanical behavior of the 22MnB5 press hardening steel was simulated using a fully coupled thermo-mechanical–metallurgical model. To accurately represent the material's response under varying forming conditions, tabulated flow curve data generated from the JMATPRO database that were consistent with the Numisheet 2008 benchmark [33–35] were utilized instead of a single continuous constitutive equation. These empirical flow curves are defined as functions of the strain, strain rate, and temperature for each individual microstructural phase. To determine the flow stress at any specific thermo-mechanical state during the simulation, a multi-dimensional linear interpolation was dynamically employed across these discrete data points.

During the simulation, a remeshing condition was applied as the deformation progressed to maintain the element quality under severe distortion. Since the deformation behavior is highly sensitive to the evolving temperature distribution and strain rate, relying

on comprehensive library data which incorporates a wide range of validated experimental results is generally more reliable than constructing flow stress curves from a limited set of experimental datasets. These established, validated experimental data offer better consistency and repeatability across diverse thermomechanical conditions. For this reason, the simulation utilizes the default material parameters from the Simufact library. Given the extensive volume of data within this database, presenting the entirety of the flow curves is impractical; thus, only a representative selection illustrating the relationship between the equivalent plastic strain and equivalent stress is provided in Figure 12. In the analysis, the simulation model was simplified by using a single plate for the upper and lower dies.

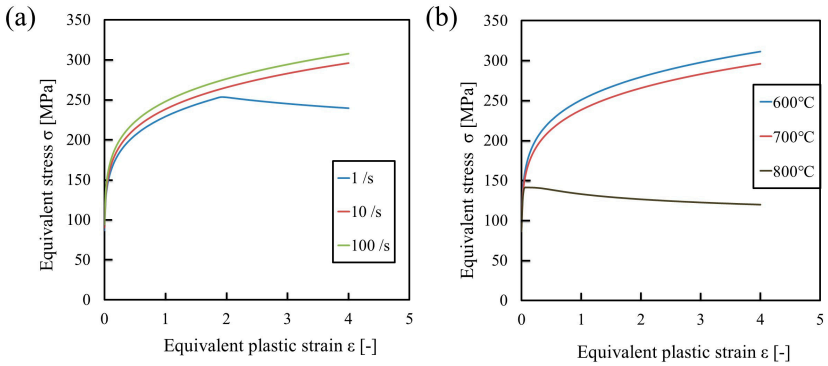


Figure 12. The relationship between the equivalent stress and equivalent plastic strain used in simulation from the Simufact program library. Adapted from Ref. [33]: (**a**) temperature t = 700 °C at each strain rate and (**b**) strain velocity $\dot{\varepsilon} = 10\ s^{-1}$ at each temperature.

The specimen used had the same dimensions as those in the experiment, and a model with the same projected shape as the punch used in the experiment was prepared. After the start of forming, the punch and the upper die were moved with the same motion at 25 mm/s. As shown in Figure 13, the simulation model for the circular punch, the tools were treated as rigid bodies and only heat transfer analysis was performed. The test pieces were treated as elastic–plastic bodies, and deformation and heat transfer analysis were performed. Also, the initial temperature of the test pieces for the simulation was 750 °C, because the temperature dropped after transferring from the furnace, as measured by thermocoupling, and the temperature of the tools and environment was 20 °C. The mesh was divided into hexahedral elements, with the upper test piece meshed at a size of 0.62 mm in the plate width direction of 0.62 mm, and in the longitudinal direction of 0.55 mm in the plate thickness direction, and the lower test piece meshed at a size of 0.67 mm in the plate width direction, 0.67 mm in the longitudinal direction, and 0.55 mm in the plate thickness direction.

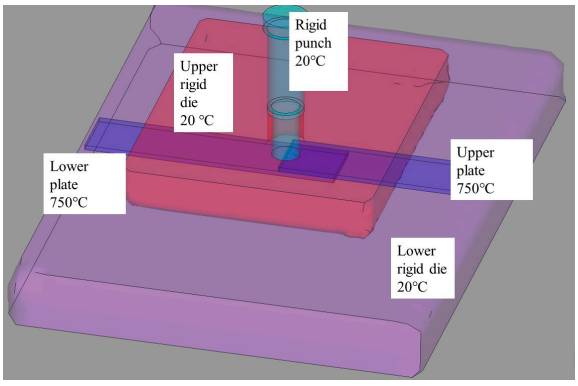


Figure 13. Finite element simulation with circular punch.

2.3.1. Material Modeling and Phase Transformation Kinetics

To implement this extensive dataset during the hot stamping simulation [32,33], the macroscopic effective flow stress ($\bar{\sigma}$) of the multiphase material at any given integration point is dynamically calculated using a linear rule of mixtures. This approach computes the sum of the flow stresses of all individual phases, weighted by their respective volume fractions:

$$\bar{\sigma}\left(\bar{\varepsilon}, \dot{\bar{\varepsilon}}, T\right) = \sum_{i=1}^{n} X_i \, \sigma_i \left(\bar{\varepsilon}, \dot{\bar{\varepsilon}}, T\right) \quad (2)$$

where X_i and σ_i are the volume fraction and the specific flow stress of the i^{th} phase, respectively. $\bar{\varepsilon}$ represents the effective plastic strain, $\dot{\bar{\varepsilon}}$ is the strain rate, and T is the temperature. To determine the instantaneous microstructural state, the phase evolution during the forming and quenching stages is continuously updated, based on its thermal history. For diffusional transformations occurring during the cooling process, the phase volume fractions are governed by the Johnson–Mehl–Avrami–Kolmogorov (JMAK) kinetics model:

$$X_d(T, t) = X_{eq}\left[1 - \exp\left(-b(T)\, t^{\,n(T)}\right)\right] \quad (3)$$

where X_{eq} denotes the equilibrium volume fraction, and $b(T)$ and $n(T)$ represent temperature-dependent kinetic parameters.

Conversely, for the diffusionless martensitic transformation, which predominantly dictates the final mechanical properties of the hot-stamped components, the empirical Koistinen–Marburger (K-M) relationship is applied when the temperature drops below the martensite start temperature (M_s):

$$X_m = X_a\left[1 - \exp(-\alpha(M_s - T))\right] \quad (4)$$

where X_a is the volume fraction of the remaining austenite prior to the transformation, T is the instantaneous cooling temperature ($T < M_s$), and α is the martensite evolution rate constant. This multiphase material modeling strategy ensures that the finite element simulation accurately captures both the thermal softening and the microstructural hardening effects throughout the entire hot forming process.

2.3.2. Theoretical Framework of Interfacial Interaction

The numerical treatment of the interface was characterized by the interplay between the mechanical stress and kinematic surface deformation. This approach accounts for the contact pressure and surface expansion rate, both of which are vital to solid-state bonding [21]. The contact interaction was governed by the contact stress (P_n), implemented using the Augmented Lagrangian formulation [34]. This method combines the advantages of the penalty method and Lagrange multipliers to satisfy the non-penetration condition with high numerical precision. The contact pressure is iteratively updated as follows:

$$P_n^{(i)} = P_n^{(i-1)} + E_n\, g_n^{(i)} \quad (5)$$

where $P_n^{(i-1)}$ represents the Lagrange multiplier (the pressure state from the previous iteration), which stabilizes the convergence. E_n denotes the contact stiffness, and $g_n^{(i)}$ is the gap function representing the localized penetration between the sheets. Physically, this iterative adjustment ensures that a sufficient counterforce is applied to prevent numerical overclosure, effectively simulating the intense compressive environment required for forge joining.

Simultaneously, the Surface Expansion rate (φ) was utilized as a kinematic indicator to quantify the generation of fresh metallic surfaces during the joining process [33]. This

parameter describes the percentage variation in the surface area of the workpiece boundary elements, defined by the following relationship:

$$\varphi = \frac{A_i - A_0}{A_0} \times 100 \quad (6)$$

where A_i is the current surface area and A_0 is the initial surface area. As the substrate undergoes significant plastic deformation and lateral flow, the surface elements are stretched, leading to a positive expansion ratio. From a physical standpoint, this expansion represents the fragmentation of brittle interfacial layers, such as oxides or Al-Si coatings. The synergy between high localized contact stress, which ensures intimate contact, and a significant surface expansion rate, which reveals virgin metallic atoms, constitutes the fundamental mechanism for achieving a successful solid-state bond at the interface.

3. Results and Discussion

3.1. Influence of Punches with Different Shape on Joint Strength

This investigation focused on the correlation between punch geometry and the resultant joint tensile strength. Figure 14 displays the outlines of the produced joints. The compression ratio (s) was fixed at 60%. Punches with circular, rectangular, and cross-shaped geometries were employed, all with the same projected area. Further experiments were conducted where the rectangular and cross-shaped punches were rotated by 45°.

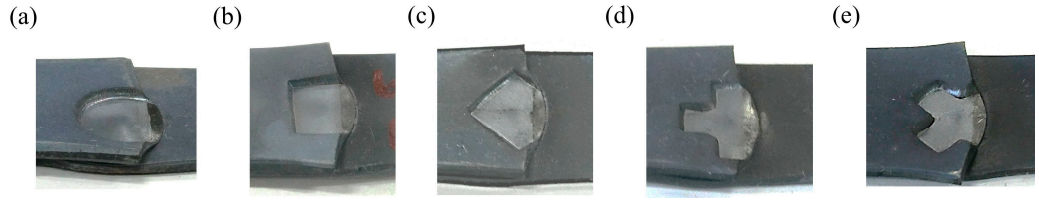


Figure 14. Joined specimen of each punch projection shape: (**a**) circle; (**b**) rectangle; (**c**) rectangle 45°; (**d**) cross; and (**e**) cross 45°.

As is evident in Figure 14, the area where the punches joined the materials exhibited a silver hue color, contrasting with the surrounding bluish-black regions. This color difference appears because the compressive plastic deformation forced the superficial bluish-black alloy layer outward, revealing the underlying steel. Moreover, in all specimens, the upper plate's edge deformed, bulging outwards. This outward deformation resulted from the upper plate being compressed and indented by the punch's shape, causing material from the indented zone to flow towards the edges. While the extent of the material flow varied with the punch's geometry, the shape of the extruded material remained consistent across all tests. Furthermore, as shown in Figure 15, the projection shape of the punch and the actual shape of the joined part almost matched, indicating high formability.

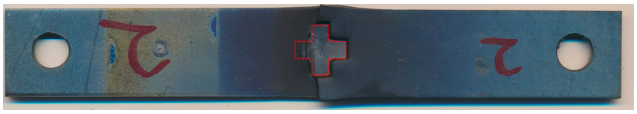


Figure 15. Overall appearance and punch compression joined by cross punch (red line).

Additionally, Figure 16a illustrates the cross-sectional profile of a specimen joined with a circular punch, obtained by cutting a test piece joint in the width direction at the compression center. In the compressed zone, the upper plate exhibited a non-uniform thickness, being thinnest at the center and gradually thickening towards the periphery. Conversely, the lower plate was thickest centrally and thinned out towards the edges. Despite these

individual thickness variations, the total thickness of the joined piece remained consistent within the punch compression area. Figure 16b, which depicts the equivalent stress distribution under identical conditions, as determined by a finite element simulation, reveals a concentration of high pressure at the center of the punch contact area. Consequently, we infer that the material in this high-pressure central region was displaced outwards towards the edges of the compression zone, leading to the observed cross-sectional shape.

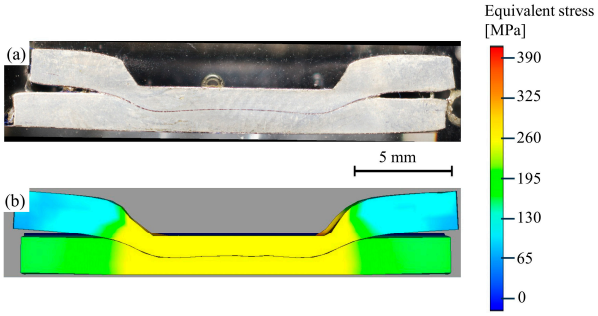


Figure 16. Cross section: (**a**) cross-section around the circular punch compression section from experiment, and (**b**) equivalent stress distribution of a cross section around a circular punch compression part in the finite element simulation.

The evaluation of joint strength was conducted by using a tensile shear test. During this test, all specimens failed by separation at the joint interface. Figure 17 illustrates the appearance of the test pieces after this separation failure for each punch type. The joined surfaces also revealed the underlying steel base material, which was consistent with observations in the punch contact area. Moreover, the exposed steel regions on the upper and lower plates were aligned, suggesting that the joining process involves the upper and lower plates pressing material against each other at their interface. The separated surfaces exhibited a rough texture characterized by fine irregularities, which we attribute to the partial fracturing of the joined layers during the separation process.

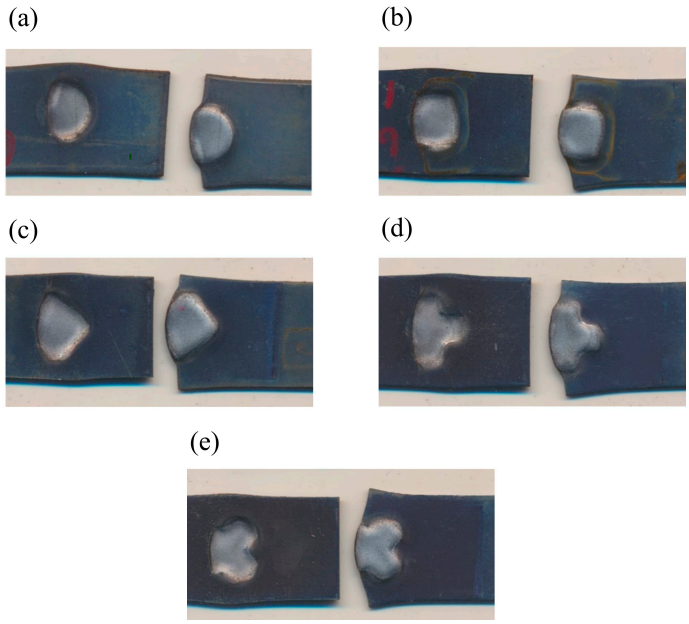


Figure 17. Separated specimens after tensile shear test: (**a**) circle; (**b**) rectangle; (**c**) rectangle 45°; (**d**) cross; and (**e**) cross 45°.

Tensile shear tests on the test pieces joined with each punch yielded stroke-load curves, as shown in Figure 18. The load increased smoothly and constantly until separation occurred in all punch conditions, suggesting that separation progressed rapidly. Overall, as the tensile shear load increased, the stroke until separation tended to increase, with the test piece using the cross-shaped punch, which showed the highest load, also exhibiting the largest stroke. When comparing the circular, rectangular, and 45°-rotated rectangular punches, which showed similar loads, the stroke until separation differed, with the rectangular punch being the largest, followed by the 45°-rotated rectangular and then the circular punch. Up to a stroke of 0.1 mm, the values were almost the same for all punch shapes, but at the 0.2 mm point, the slope already showed a significant change. The key distinction between these geometries lies in how the contact zone resists separation. The rectangular punch provides a wider projected width, perpendicular to the loading axis, facilitating a more uniform distribution of shear stress compared to the concentrated shear stress of circular punches. This broader front allows for more extensive deformation across the upper specimen before interfacial separation begins. Although this results in a shallower slope, the geometry effectively delays the initiation of joint debonding. Therefore, this rectangular configuration leads to enhanced joint strength, ultimately resulting in higher maximum tensile shear loads.

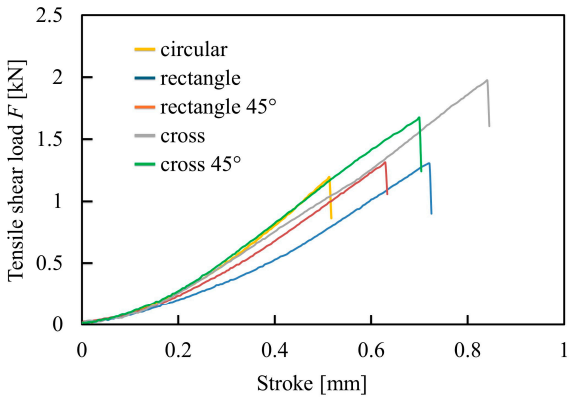


Figure 18. Tensile shear load–stroke curves in each punch projection shape.

The maximum load just before separation, obtained from the tensile shear tests, is defined as the joint strength (maximum tensile shear load). The relationship between the punch projection shape and the joint strength is shown in Figure 19; the tensile shear load increased in the following order: circular punch, rectangular punch, and then cross-shaped punch. On the other hand, rotating the punch by 45° did not yield a significant overall effect, but for the rectangular punch, the test pieces using the 45°-rotated punch showed less variation in values. However, considerable scatter was still observed in some test conditions. This variability can be attributed to several experimental factors. First, slight fluctuations in the delivery time from the heating furnace to the die could affect the initial temperature of the specimens, leading to minor temperature gradients. Second, minor alignment issues during the joining process could cause the joint to form off-center, thereby altering the initial joining surface area. Lastly, material inconsistencies, such as variations in the initial coating thickness, could influence the joint formation. To mitigate these issues in future work, automated transfer mechanisms could be implemented to strictly control the delivery time and temperature, alongside the use of self-aligning grips for testing and stricter pre-screening of specimen coating thicknesses.

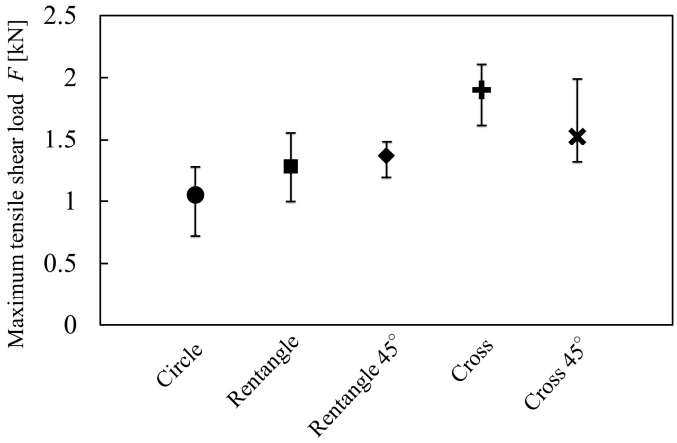


Figure 19. Relationship between maximum tensile shear load and punch projection shape.

Through investigating the relationship between the perimeter of each projection shape and the joint strength, the contribution to the improvement of joint strength was considered, specifically by examining its relationship for two types of perimeters. Figure 20a shows the total perimeter of the punch tip used for compression (red line). Figure 20b shows the perimeter of the part contacting the upper plate (red line); the figure shows the rectangular punch and the test piece as viewed from above, with the specimen stacked. Due to the elastic deformation, the set compression ratio of 60% was about 45% for the real compression ratio, and the punch is hypothesized to have contacted the upper specimen exclusively, without contacting the lower specimen. In summary, the total perimeter increased in the order of circular, rectangular, and cross-shaped. However, for the part of the punch contacting the upper plate, the perimeter increased in the order of circular, rectangular, 45°-rotated cross-shaped, and 45°-rotated rectangular designs, with the cross-shaped having the largest perimeter, and the relationship between the joint strength and the overall perimeter, which is shown in Figures 21 and 22, illustrates the relationship between the joint strength and the compressed upper plate perimeter.

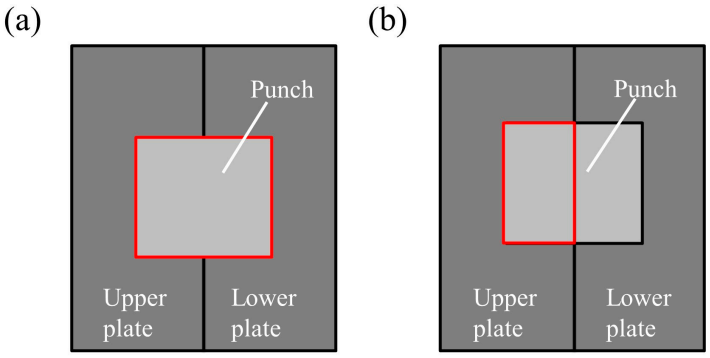


Figure 20. Perimeter of joint area (red line): (**a**) perimeter of the compression area, and (**b**) perimeter of the compression area of the upper plate.

The correlation between punch geometry and joint performance was evaluated across five distinct geometric conditions. To ensure high data integrity, each condition was validated through six independent replications, yielding a total of 30 specimens. This experimental design resulted in minimal standard deviations, indicating that the observed trends reflect the intrinsic physical characteristics of the joint, rather than experimental variability. A correlation coefficient (r) was used to determine the linear relationship between the perimeters and the tensile shear load. A positive correlation was observed for both the overall and compressed part perimeters; subsequent regression analysis yielded

coefficients of 0.74 in Figure 21 and 0.78 in Figure 22, confirming a consistently strong correlation in both cases.

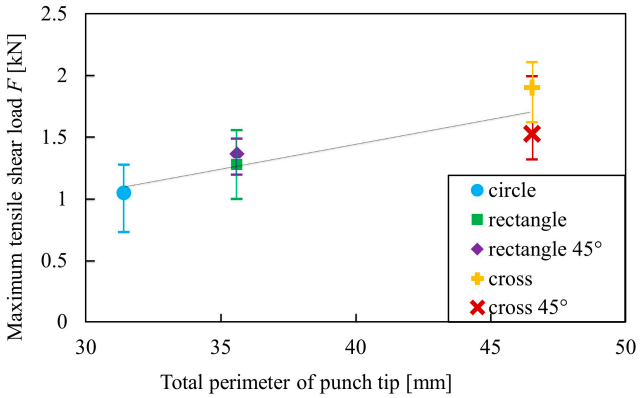


Figure 21. Relationship between tensile shear load in each projection shape and total perimeter of the punch tip.

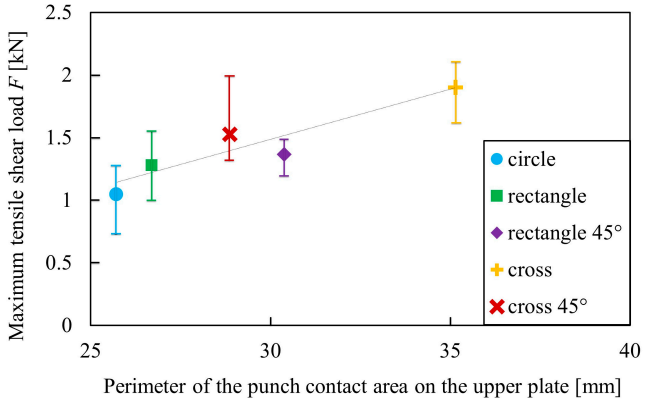


Figure 22. Relationship between tensile shear load in each projection shape and perimeter of the upper plate compression section.

3.2. Effect of Rectangular Punches with Different Aspect Ratios on Joint Strength

The effect of the aspect ratio in rectangular punches was investigated. Similar experiments were conducted by varying the aspect ratio of rectangular punches, while keeping the projected area approximately the same. Figure 23 shows the punch projection shapes and the joined specimens. The aspect ratios were 1:2, 1:1 and 2:1 (the 1:2 ratio rotated by 90°), resulting in three conditions. The appearance of the joints was similar to the specimens joined using circular, rectangular, and cross-shaped punches. However, a clear difference was observed in the amount of deformation of the upper plate. As the punch length in the width direction increased, with aspect ratios of 1:2, 1:1, and 2:1, the amount of deformation of the upper plate at the joint increased.

After the experiment, tensile shear tests were conducted to investigate the joint strength. The obtained load–stroke curves are shown in Figure 24a, and similarly to other projection shapes, the load significantly decreased after the occurrence of separation. Furthermore, the rectangular punch with an aspect ratio of 2:1, which had the highest joint strength, also exhibited the largest stroke. Additionally, the 1:1 ratio exhibited a lower initial slope in tension compared to the 1:2 ratio. This is attributed to its wider surface, perpendicular to the tensile direction, resulting in higher resistance to the force in the tensile direction. Moreover, Figure 24b illustrates the maximum tensile shear load for each aspect ratio. It shows that the 2:1 ratio has the highest load, followed by 1:2 and 1:1. However, the 1:2 aspect ratio exhibited significant variation. The relationship between

the overall perimeter, the compressed part perimeter, and the joint strength is shown in Figures 25a and 25b, respectively. The overall perimeter had a correlation coefficient of 0.44, indicating no strong correlation. On the other hand, the correlation coefficient for the compressed part perimeter was 0.90, showing a strong positive correlation. These results suggest that increasing the compressed part perimeter of the upper plate can be expected to improve the joint strength. Since the separation that occurs during the tensile test is brittle separation, the separation that initiates from the outer edge of the joint propagates immediately inward, causing the specimens to separate. As shown in Figure 26, the punch's compressed area maintains excellent shape form, and the positions of the outer edge of the punch and the outer edge of the joint coincide. Therefore, a direct correlation is observed between the length of the punch perimeter that is in contact with the upper plate and the resulting joint perimeter. This extended joint perimeter consequentially enhances the resistance to tensile forces, leading to a demonstrable increase in the overall joint strength.

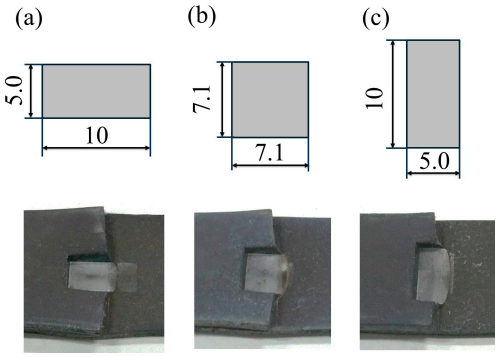


Figure 23. Rectangular punch with the same projection area and different aspect ratios (width: longitudinal direction): (**a**) 1:2; (**b**) 1:1; and (**c**) 2:1 [unit: mm].

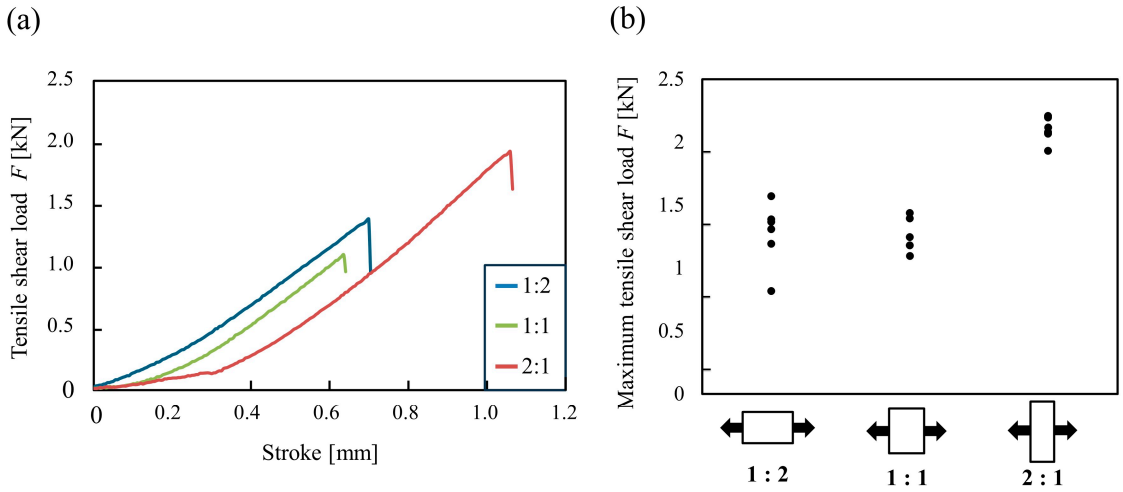


Figure 24. Tensile-shear performance of joints with rectangular punches at various aspect ratios: (**a**) load–stroke curves, and (**b**) relationship between maximum tensile-shear load and punch tip geometry (width: longitudinal direction).

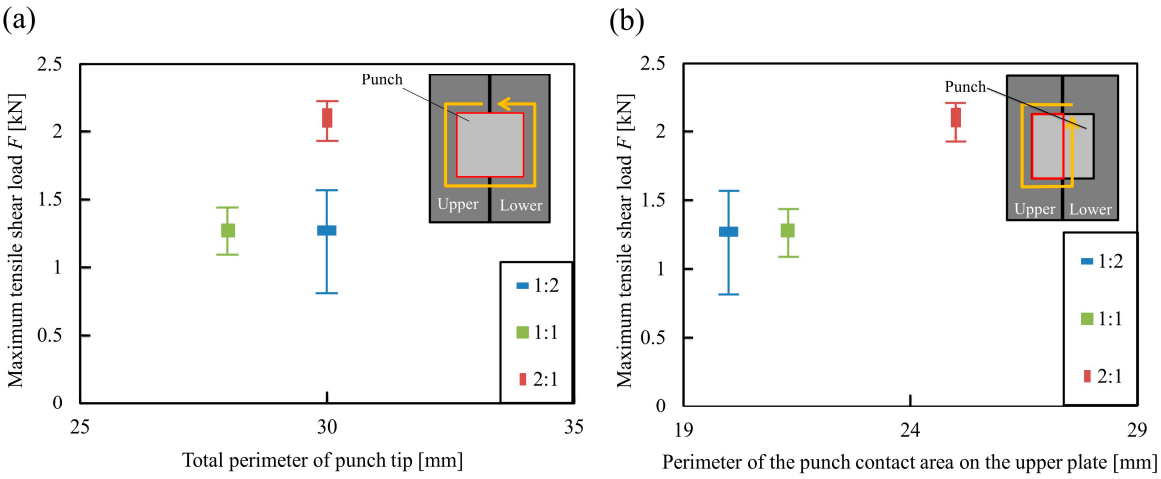


Figure 25. Relationship between maximum tensile shear load and punch geometry parameters at various aspect ratios: (**a**) total perimeter of the punch tip, and (**b**) perimeter of the punch contact area on the upper plate. Red lines and yellow arrows indicate the measured perimeters and direction, respectively.

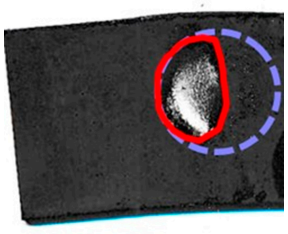


Figure 26. Joint surface of the lower specimen with a circular punch. Red: joint, and blue: punch tip.

3.3. Influence of Punch Tip Inclination Shape on Joint Strength

The changes in punch shape have been in the pressing projection direction (longitudinal direction and sheet width direction). To introduce changes in the pressing direction (sheet thickness direction) as well, the influence on the joint strength was investigated, using punches with an inclined tip. The inclined punches used had a 2° or 8° inclination at the tip, relative to a rectangular punch with a tip cross-sectional shape of 8.9 mm × 8.9 mm, as shown in Figure 27. An experiment was conducted with a compression ratio of s = 60%, using punches both with and without inclination. The joint cross-section was observed to compare the formed shapes, due to the inclination. The specimens were cut longitudinally along the center of the punch, polished, and then observed using a light microscope. As shown in Figure 28, the inclination in the punch part increased with the increasing tip inclination, indicating that sufficient formability was obtained.

Figure 29a shows the results of the tensile shear test on the joined specimens to investigate the joint strength. Although the increased inclination slightly promoted the material flow, the average joint strength was higher for the specimen without inclination. This is attributed to dissimilarities in the solid-state bonded area. As shown in Figure 28, as the inclination decreases, the unbonded area (black part) in the interfacial area decreases, indicating effective solid-state bonding. A wider range of solid-state bonding, achieved under consistent compression rate conditions, is considered to enhance the joint strength.

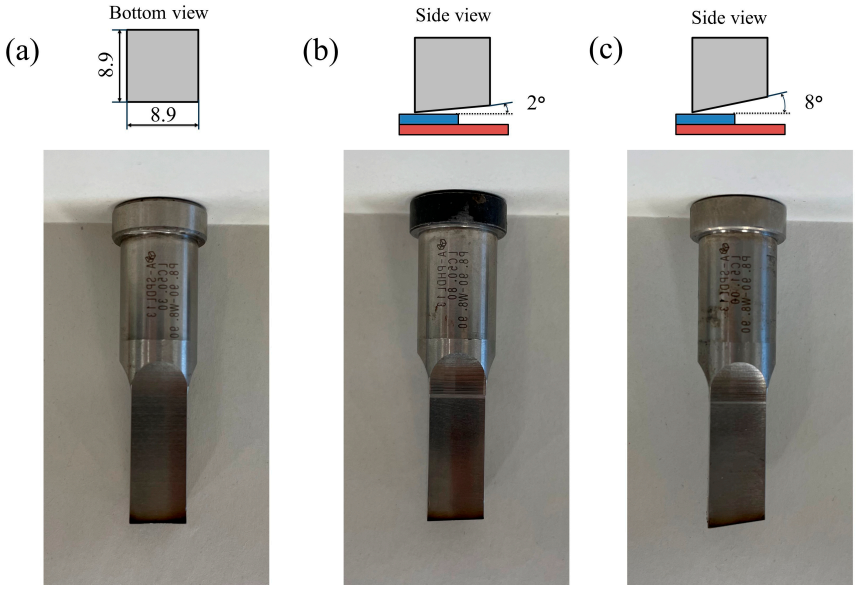


Figure 27. Punch tip with and without inclination used in the experiment: (**a**) No tilt 0°; (**b**) Tilt 2°; and (**c**) Tilt 8°. Red: lower plate, blue: upper plate, [unit: mm].

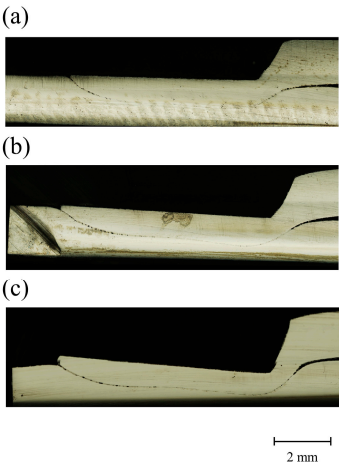


Figure 28. Cross-sectional view of joined specimen: (**a**) No tilt 0°; (**b**) Tilt 2°; and (**c**) Tilt 8°.

Mechanically, successful solid-state bonding requires uniform, high hydrostatic pressure to effectively break surface oxide layers and promote intimate interfacial contact. A flat punch 0° provides this simultaneous and uniform compression across the entire interface. In contrast, an inclined punch introduces a progressive contact mechanism, resulting in an asymmetric stress state. While the localized pressure at the initial point of contact may be high, the trailing regions fail to reach the critical hydrostatic pressure required for bonding. Furthermore, the asymmetric material flow induces interfacial slip, which can shear and disrupt the nascent metallic bonds forming during the compression stage. This combination of non-uniform compressive stress and excessive interfacial slip explains why the unbonded areas expand as the punch inclination increases.

The direction of the inclination was also investigated. The inclination of a punch can change how the force is applied to the material. A straight punch applies pressure evenly, whereas an inclined punch creates a more gradual, shearing-like force as it contacts the material. This gradual contact can be used to improve the quality of a sheared edge and reduce the forming load required to create a joint. The joint strength was investigated by rotating the 2° inclined punch's inclination direction by 90 degrees each time. As shown in Figure 29b, the average values of each joint strength were within the range of 0.7–1.3 kN,

and no significant differences were observed. From a mechanics perspective, rotating the inclined punch merely shifts the orientation of the asymmetric stress distribution and interfacial slip, but it does not alter the overall proportion of the effectively bonded area. Therefore, it was found that a significant improvement in joint strength cannot be expected by changing the direction of the inclination.

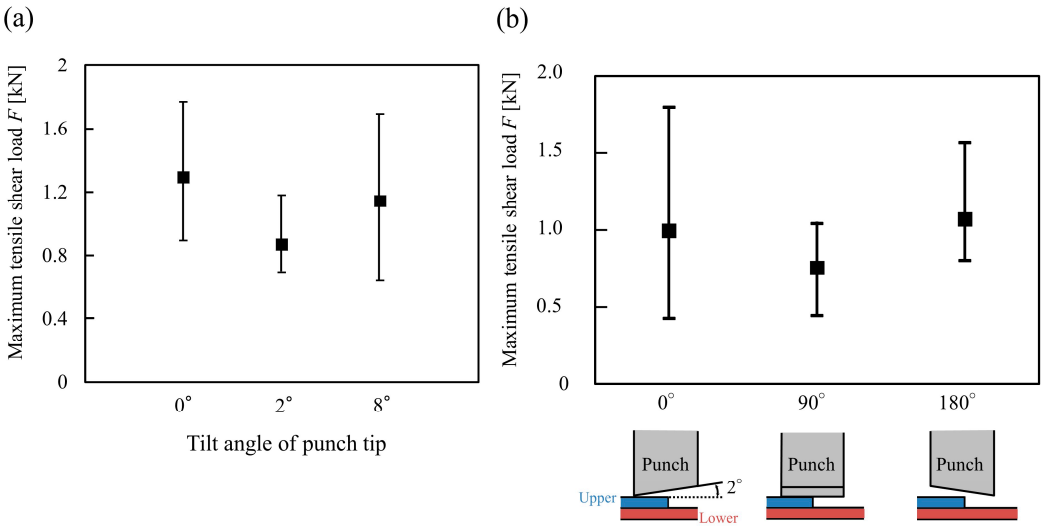


Figure 29. Influence of punch tip inclination shape on maximum tensile shear load: (**a**) variation across different tilt angles, and (**b**) influence of the tilt direction of constant 2° tilt angle. Red: lower plate, blue: upper plate.

An additional aspect of the study involved an investigation into the forces generated during the forming process. Specifically, the press load was analyzed to understand how it was affected by changes in the inclination of the forming tool. Figure 30a presents the peak press load values recorded for a range of inclination angles. Similarly, Figure 30b illustrates the peak press load values corresponding to various inclination directions.

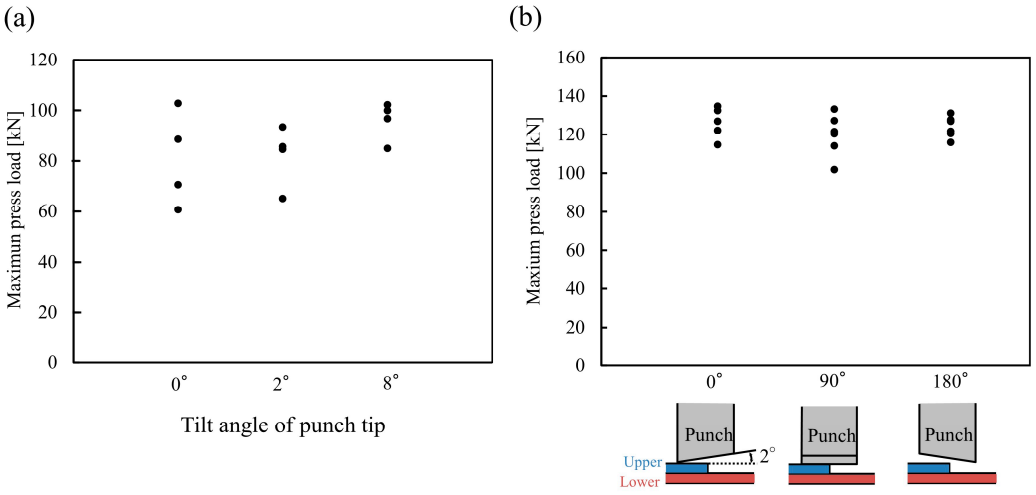


Figure 30. Maximum press load during the forge joining experiment, using a flat die: (**a**) influence of punch tip tilt angle, and (**b**) influence of the tilt direction of constant 2° tilt angle. Red: lower plate, blue: upper plate.

A key finding from this analysis was the remarkable consistency of the peak press load. The data revealed that the load did not change significantly, regardless of whether the inclination angle or the inclination direction was altered. Mechanistically, while an

inclined punch induces asymmetric material flow towards the unconstrained side during the downward stroke, the peak load is generated at the bottom dead center. At this final stage, the steel becomes fully constrained between the punch and the flat lower die. Because the total projected contact area and the volume of the plastically deformed material remain constant across all inclination setups, the total plastic work required to complete the joining process is conserved. Consequently, the localized redistribution of stress at the inclined punch tip is overridden by the bulk flow stress of the material. This led to the conclusion that a reduction in the forming load cannot be effectively achieved by simply modifying the inclination shape or direction. These results suggest that the primary factors influencing the forming load are dictated by the invariant macroscopic boundary conditions, rather than the localized punch geometry.

4. Forming Analysis of Finite Element Simulation

4.1. Analysis of the Influence of Punch Geometry on Joint Strength

Simulations were performed using CAD models of circular, rectangular, and cross-shaped punches under the same conditions as the 60% compression ratio in the experiment. In the obtained analysis results, the distributions of the contact pressure and surface expansion rate at the bottom dead center were compared for each punch shape. To ensure the reliability of the numerical results, the FE model was calibrated and validated against the experimental data. For each tested condition, the simulated thickness calculated using the actual compression ratio was precisely matched to the average joint thickness measured from the experiments, which served as the primary benchmark. The deviation between the experimental and simulated thickness was strictly maintained within 5%.

This calibration process ensures that the material flow and boundary conditions in the simulation are consistent with the physical joining process. Since the material flow is governed by the principle of volumetric constancy, this high degree of geometric agreement in the thickness profiles confirms that the model accurately captures the plastic strain and the resulting surface expansion rate. Consequently, this geometric validation approach serves as a reliable indicator of the overall deformation behavior at the interface.

Figure 31 left column illustrates the equivalent stress distribution across the width-wise cross-sections for circular, rectangular, and cross-shaped punch joints. The simulation results indicate that equivalent stress is distributed throughout the specimen within the compressed region beneath the punch. For all three geometries, the stress distribution remains uniform, relative to the compression direction, with values generally increasing toward the center of the punch. Notably, the cross-shaped punch exhibited slightly lower stress values at the center compared to the circular and rectangular designs, though this difference was not statistically significant. However, further observation is required to determine how the uniformity of contact pressure relates to these stress profiles, as consistent pressure across the interface potentially represents a critical determinant for achieving solid-state bonding. As shown in Figure 31 right column, the surface expansion rate is distributed across the interfacial area. This expansion rate serves as an indicator of the solid-state bonding region, where an increased surface area facilitates the bonding process.

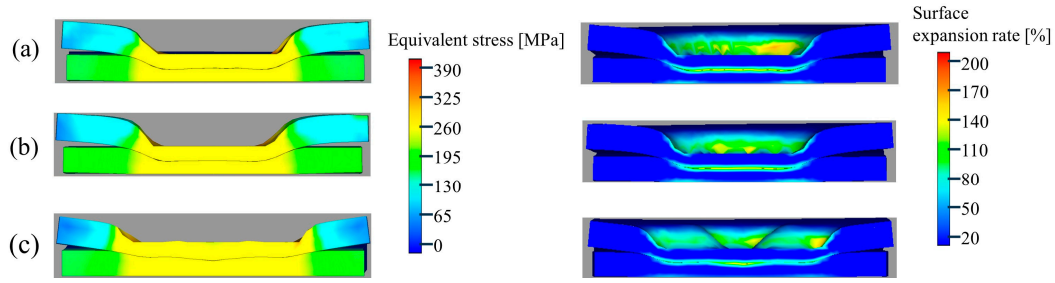


Figure 31. FEA results of central cross-sections for various punch geometries: (**a**) circular punch; (**b**) rectangular punch; and (**c**) cross punch. The left column illustrates the equivalent stress distribution, while the right column shows the surface expansion rate distribution.

Furthermore, the distribution was only on the surface; the compression direction, as seen in contact pressure, and the internal area were not observed. Also, no clear changes were observed in the trend of distributed values or the maximum value when comparing each punch. The joint surfaces were also investigated. Figure 32 shows the contact pressure distribution on the joint surfaces of circular, rectangular, and cross-shaped punch joints in the finite element simulation. The surface expansion rate distribution in Figure 33 shows that both the upper and lower specimens had a higher contact pressure at the center of the joint than around the periphery. No significant difference in the distribution of high contact pressure was observed between the upper and lower specimens. The maximum contact pressure observed was approximately 900 MPa, and the maximum surface expansion rate was approximately 200%. Furthermore, in the experiments conducted under the same conditions, bonding was achieved with all punch shapes, and the joint strength was higher in the order of circular, rectangular, and cross-shaped punches, as shown in Figure 19. On the other hand, the simulation showed that the cross-shaped punch had relatively lower contact pressure and surface expansion rate distributed. Therefore, it was found that the magnitude of the maximum or average values of contact pressure and surface expansion rate is not the determining factor for the strength of the joint, and bonding can be achieved if there is a certain level of contact pressure and surface expansion rate.

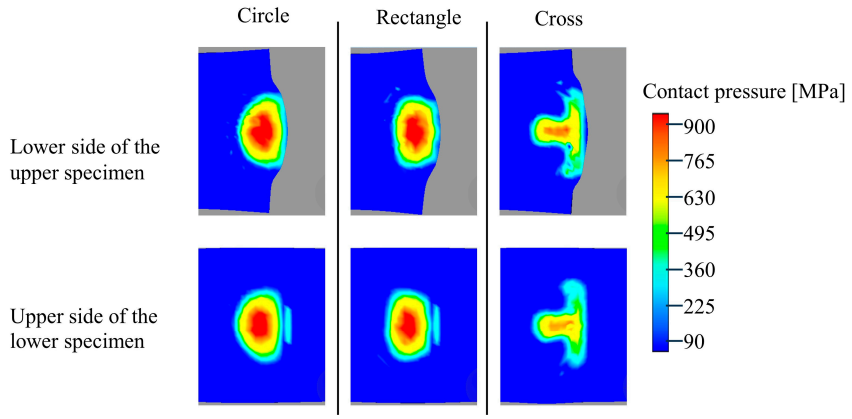


Figure 32. Contact pressure distribution at specimen joint surfaces in finite element simulation, using circular; rectangular; and cross punches.

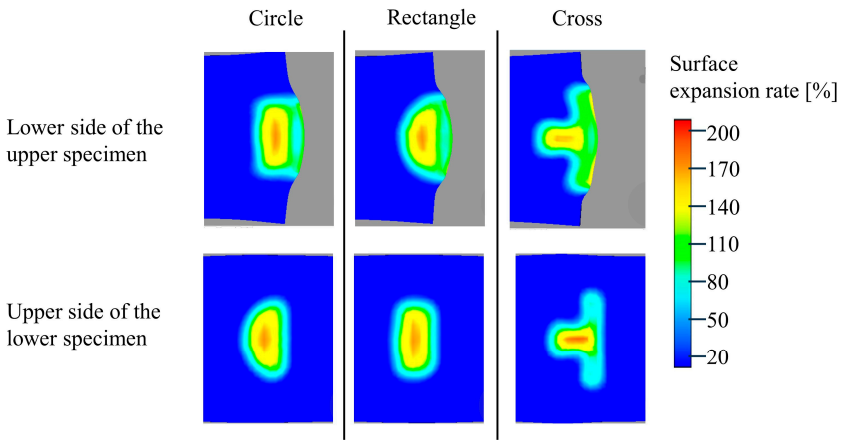


Figure 33. Surface expansion rate distribution at specimen joint surfaces in finite element simulation, using circular; rectangular; and cross punches.

4.2. Analysis of the Effect of Rectangular Punch Aspect Ratios on Joint Strength

Similar simulations were also performed for rectangular punches with different aspect ratios. Figure 34 shows the contact pressure distribution for the 1:1, 1:2, and 2:1 rectangular punch joints in the finite element simulation, and Figure 35 shows the surface expansion rate distribution. Similar to the circular and cross-shaped punches, the 1:1 and 1:2 rectangular punches showed a high contact pressure and surface expansion rate ratio at the center of the joint in both the upper and lower specimens. On the other hand, the 2:1 rectangular punch, which had a relatively high joint strength, tended to show a uniform distribution. Contact pressures of around 600 MPa and a surface expansion rate of around 120% were distributed over a wide area. Experimental results for the 2:1 rectangular punch showed the highest joint strength, validating the simulation trends for all three punch shapes. According to the finite element analysis, this superior performance is due to the 2:1 punch exhibiting a more uniform distribution of lower maximum contact pressure and a reduced maximum surface expansion rate compared to the other geometries.

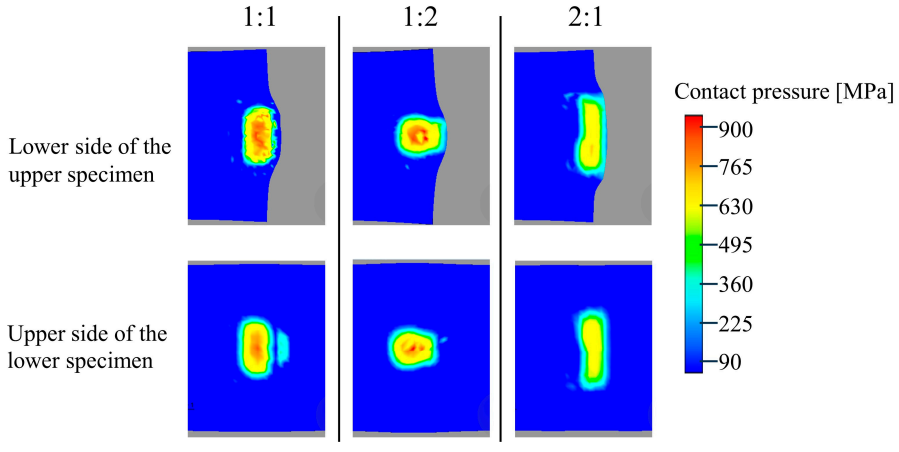


Figure 34. Contact pressure distribution at specimen joint surfaces in finite element simulation, using rectangular punch with aspect ratio (width: longitudinal direction) of 1:1; 1:2; and 2:1.

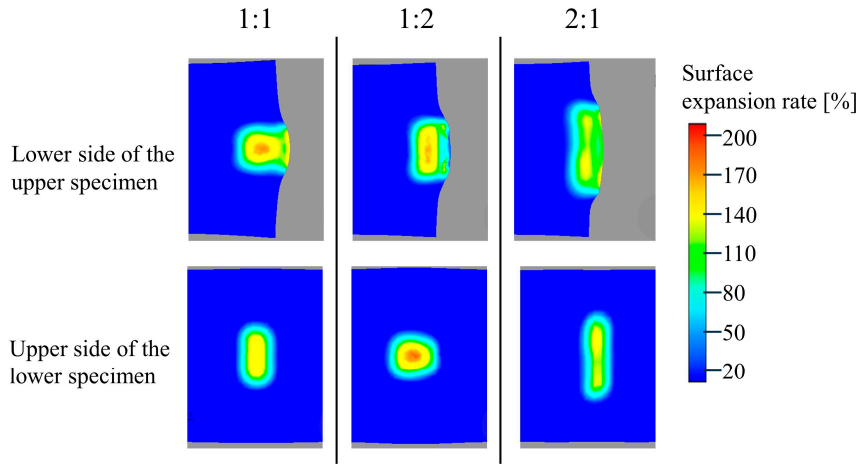


Figure 35. Surface expansion rate distribution at specimen joint surfaces in finite element simulation, using rectangular punch with aspect ratio (width: longitudinal direction) of 1:1; 1:2; and 2:1.

4.3. Analysis of the Influence of Punch Tip Inclination on Joint Strength

Finite element simulations were also performed for punches with and without inclination. Using models with the same dimensions as the punches used in the experiment (0° inclination and 2° and 8° inclinations), forming analysis was conducted, and the contact pressure and surface expansion rate were investigated. Figure 36 shows the contact pressure distribution for inclined punch (0°, 2°, 8°) joints in the finite element simulation, and Figure 37 shows the surface expansion rate distribution. Both the upper and lower specimens showed higher contact pressure at the center of the joint than around the periphery. In the joint, no significant difference in the distribution of contact pressure was observed between the upper and lower specimens. On the other hand, the surface expansion rate distribution at the center of the joint increased with the increasing inclination, and values exceeding 200 MPa were observed in the distribution for the 8° inclined punch. In mechanical terms, such a drastic increase in the surface expansion rate denotes intense sliding at the interface. The inclination of the punch results in an uneven stress distribution, driving the lateral material flow and hindering stable solid-state bond formation.

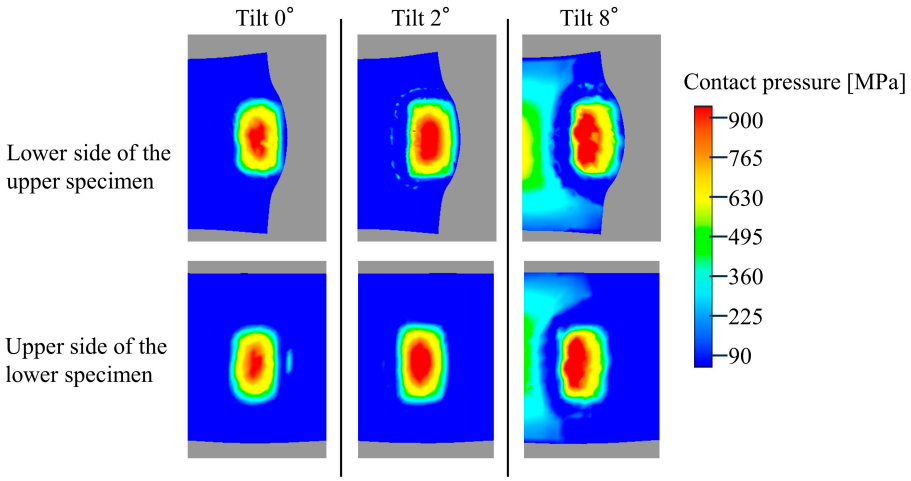


Figure 36. Contact pressure at specimen joint surfaces in finite element simulation, investigated using a tilt rectangular punch with slopes of 0°; 2°; and 8°.

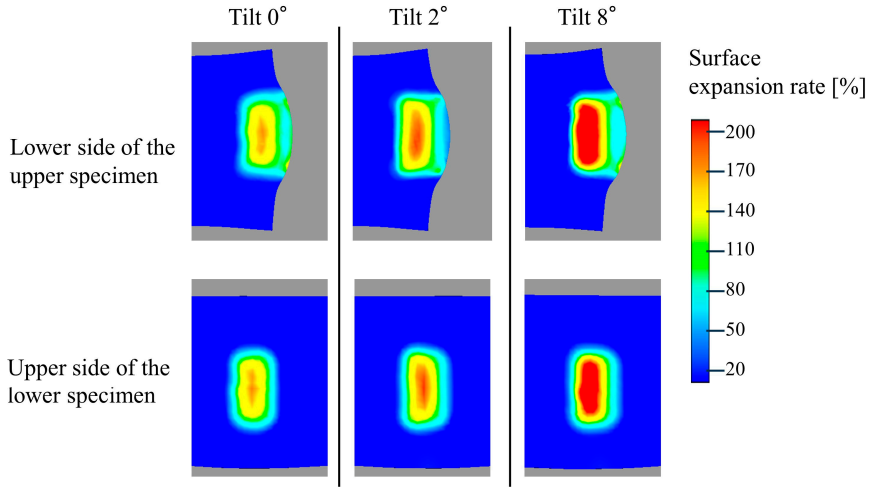


Figure 37. Surface expansion rate distribution at specimen joint surfaces in finite element simulation, investigated using a tilt rectangular punch with slopes of 0°; 2°; and 8.

Based on the simulation results obtained for various punch geometries, under conditions of equivalent projected punch area, punch shapes with a relatively uniform distribution of contact pressure and surface expansion rate values tended to exhibit higher joint strength. This tendency was strongly evident in the contact pressure distribution, showing this trend across all conditions. A uniform contact pressure distribution implies a stable and symmetric hydrostatic stress state at the interface. This condition minimizes detrimental interfacial slip, as evidenced by the lower surface expansion rates, and ensures that the applied force promotes solid-state bonding, rather than lateral shearing.

5. Hot Stamping Experiments of Forge Joining Using Hat-Bending Die

The dimensions of the hat-bending die and the test specimen used in the experiment are shown in Figure 38; the specimen material is a 22MnB5 Al-Si-coated steel plate. The dies were fabricated from SKD11 (cold-work tool steel) and tempered to induce hardening, ensuring high thermal stability and toughness during the hot stamping process and S50C (carbon steel) for the rest. To stabilize the transport, two 7 mm diameter positioning pins were installed at specific locations on the die to ensure that the steel sheet was placed in a fixed position. The clearance for the hat-bending section was designed to be 3.2 mm, which is the combined thickness of the two overlapped steel sheets. As shown in Figure 39, a hot stamping hat-bending test was first performed without installing the punches to confirm formability. This experiment utilized the same parameters as the forge-joining setup for the strip plate shown in Figure 3, with a compression ratio of 60%. The patch specimens were positioned so that their 163.4 mm side faced the die's width, and their 128 mm side faced the longitudinal direction. For the hole radius, an 8.6 mm hole was created at a specific position on the test specimen, and accurate positioning was achieved by inserting a positioning pin into this hole and forming began within 3 s. The forming process continued until the edges of the sheet were bent into the hat shape, after the entire sheet was compressed in the pressing direction by the die. Upon reaching the bottom dead center, the specimens was die quenched, causing its temperature to drop rapidly. By the time the bottom dead center hold ended, the entire sheet had turned black. The cooling rate was observed to be fastest on the outer edges and to gradually slow toward the center. The peak press load reached approximately 40 kN upon reaching the bottom dead center. Initial tests conducted without punch installation confirmed excellent formability; the specimens accurately conformed to the die geometry with no observable springback.

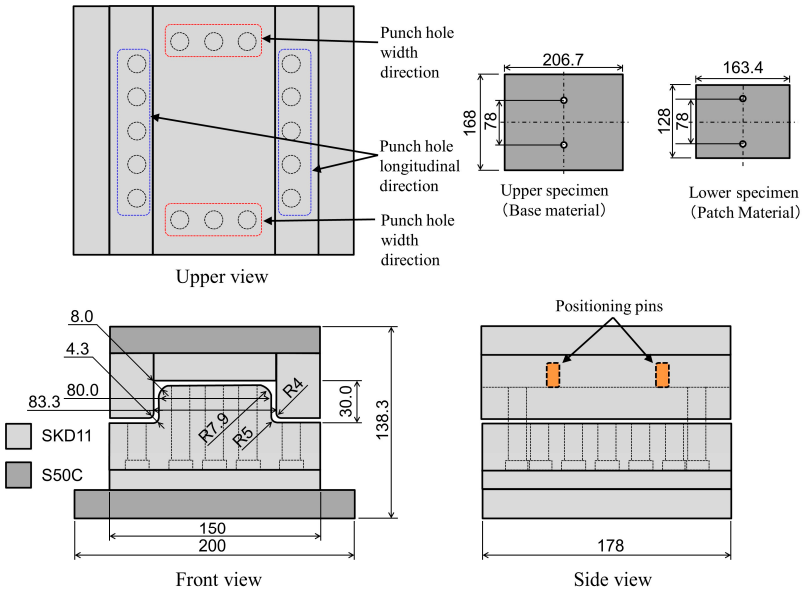


Figure 38. Geometric specifications and dimensions of the hat-bending die and patchwork blank specimens designed for the forge joining of patchwork blanks during the hot stamping process [unit: mm].

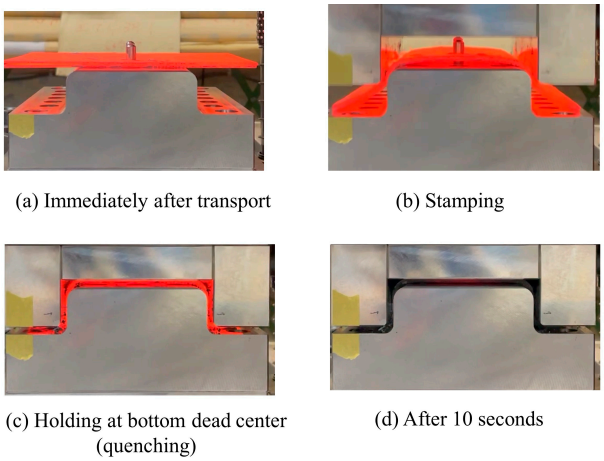


Figure 39. Hot stamping process for 22MnB5 steel plates, using a hat-bending die without a punch insert.

Hot stamping was conducted by placing punches in the lower die during hat bending. The punch installation positions in the lower die are shown in Figure 40. Experiments were performed under two conditions: in Figure 40a, one using a total of four holes was located only in the center of each side, and another used a total of eight holes, as shown in Figure 40b, with two on each side. The punches were set at a compression ratio of s = 60% for the combined sheet thickness of 3.2 mm. The material used was Al-Si-coated material. This prevented the formation of an oxide scale, allowing for compression with a high surface quality.

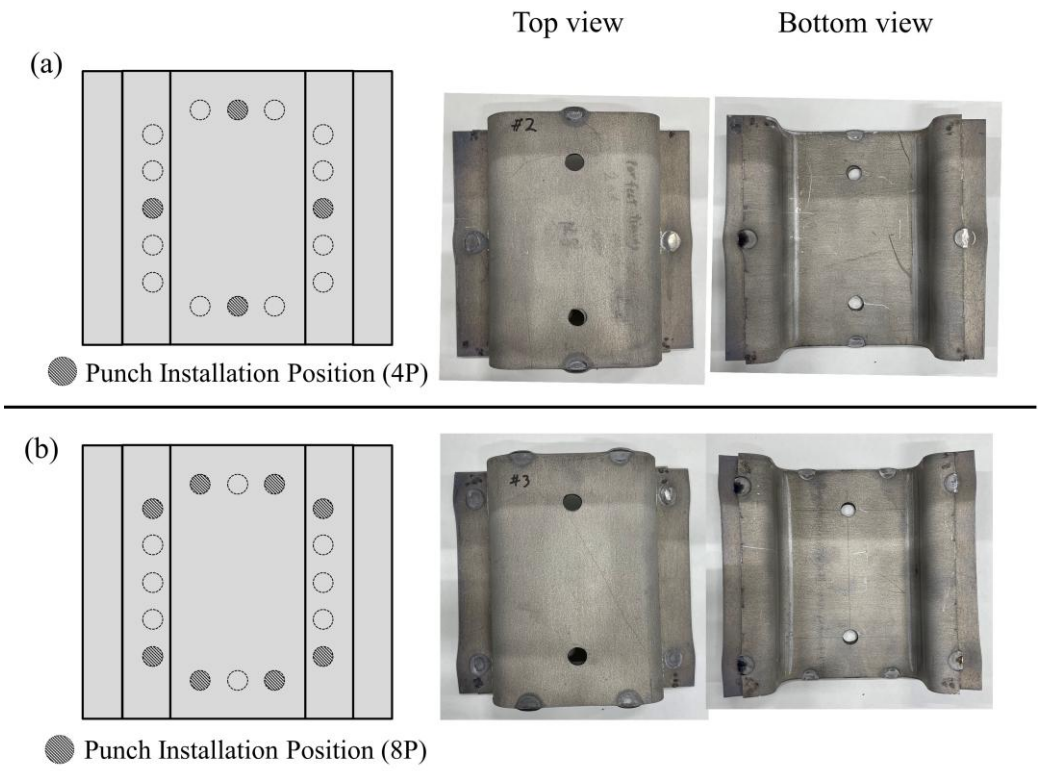


Figure 40. Experimental setup and resulting specimen appearances after hot stamping with hat bending: the (**a**) four-punch configuration, and (**b**) eight-punch configuration. Each panel illustrates the punch installation positions in the lower die alongside the corresponding top and bottom views of the joined specimens.

Figure 40 shows the external appearance of the specimen after forming. On the joined surface, the base metal was exposed on the hat-bending side walls and at the punch compression points, where the silvery Fe layer was visible. No gaps were observed between the upper and lower sheets at the compressed areas, suggesting that a good joining state was achieved. The thickness of the compressed areas was measured with a micrometer, and the actual compression ratio was calculated from the punches. The average actual compression ratio was 37.3% for the condition with four punches and 32.2% for the condition with eight punches. Compared to similar experiments using a flat die, the actual compression ratio was about 5% lower with four punches and about 10% lower with eight punches. The difference in the actual compression ratio due to the number of punches is thought to have been caused by the punch locations. In the condition with four punches, this is located in the center, allowing the material to easily flow toward the periphery. In contrast, in the condition with eight punches, this is located at the ends, which likely made it difficult for the material to be pushed in both directions. This is why a difference in the actual compression ratio was observed. The peak press load was approximately 300 kN for the four-punch condition upon reaching the bottom dead center and 470 kN for the eight-punch condition.

Analysis of Forge Joining Using Hat-Bending Die

In each of the joined specimens, the achievement of joining through the forge joining process was investigated. Figure 41 shows the specimens after cutting. As shown in Figure 41a, the samples were cut at specific points, using a bandsaw. This eliminated the mechanical joining that occurred at the corners, allowing for an accurate evaluation of the forge joining quality. Figure 41b shows that the specimen with four punches remained joined across its entire length, even after cutting. This suggests that effective forge joining

was achieved at all punch compression points. In contrast, Figure 41c shows that the eight-punch specimen yielded a different result. While forge joining was successful at both ends, the central section easily separated after the cut. This indicates that robust forge joining was only achieved at the two ends.

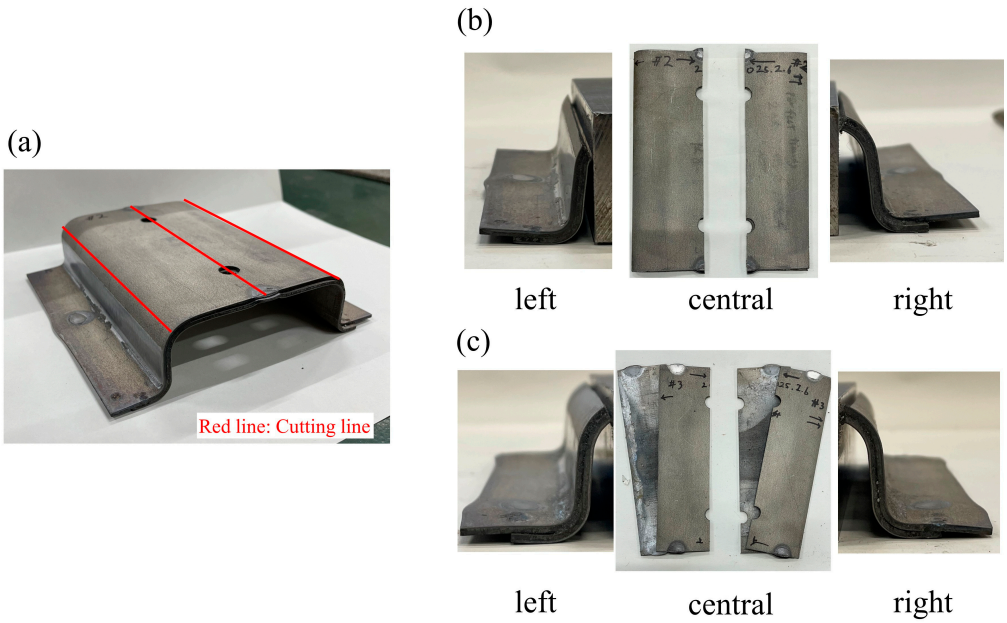


Figure 41. Cross-sectional analysis of joined Al-Si-coated 22MnB5 steel plates: (**a**) cutting positions indicated by red lines; specimens joined by hat bending using (**b**) 4 punches; and (**c**) 8 punches.

The difference in the joining quality is directly correlated to the actual compression ratio, which was about 5% lower in the eight-punch specimen. To quantitatively address the underlying causes of this reduction, the forming loads were decoupled into their bending and joining components. Preliminary tests indicated that the load required solely for the hat-bending process, prior to punch engagement, is approximately 40 kN. By subtracting this bending load from the peak press loads, the effective forging load distributed among the punches, $F_{effective}$, can be calculated as follows:

$$F_{effective} = \frac{F_{total} - F_{bending}}{n} \quad (7)$$

where F_{total} is the peak press load, $F_{bending}$ is the load consumed by the bending operation (40 kN), and n is the number of punches. Based on these calculations, Figure 42 was plotted to elucidate the relationship between the applied loads and the process efficiency, comparing the hat-bending configurations with a baseline flat-die experiment. Figure 42a demonstrates the global effect of the total press load on the actual compression ratio. As the total force massively increases from 300 kN (four punches) to 470 kN (eight punches), the graph shows a clear downward trend in the actual compression ratio. This inverse relationship indicates that the elevated total loads inevitably induce greater elastic compliance in the tooling setup. Consequently, a significant portion of the press stroke is absorbed by this elastic tool deflection, leading to a shallower actual compression ratio.

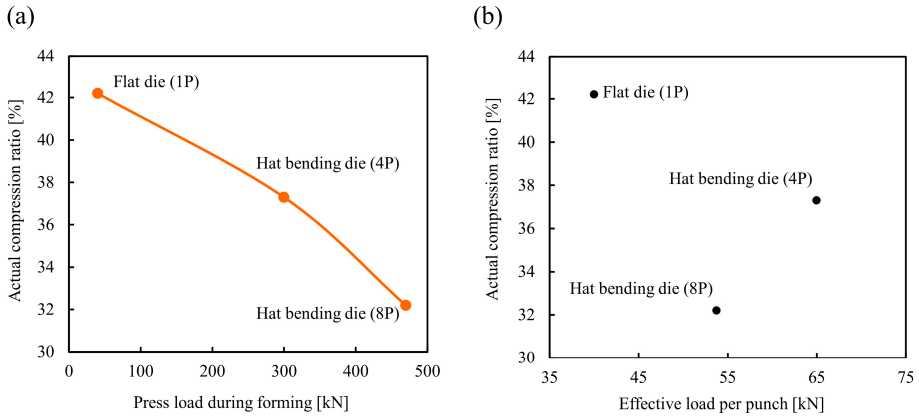


Figure 42. Analysis of process efficiency: (**a**) relationship between the total press load and actual compression ratio, illustrating the adverse effect of elastic tool deflection, and (**b**) relationship between the effective load per punch and actual compression ratio, highlighting the material flow constraints in the hat-bending die compared to the flat die baseline.

Furthermore, Figure 42b highlights how the hat-bending geometry imposes severe material flow constraints. In the unconstrained flat die baseline, an effective load of only 40 kN per punch was sufficient to achieve the 42.2% actual compression ratio. In contrast, the four-punch hat-bending setup required a substantially higher effective load of 65 kN per punch, but only achieved a 37.3% actual compression ratio. This discrepancy occurs because the material in the hat-bending die is highly confined by the bent side walls, drastically increasing the flow stress.

This constraint effect is critically exacerbated in the eight-punch condition. As illustrated in Figure 42b, despite having the highest total press load, the effective load drops to 53.75 kN per punch, coinciding with the lowest actual compression ratio of 32.2%. In this configuration, the high density of punches causes severe inter-punch material flow interference along the longitudinal axis. While the punches located near the ends benefit from adjacent free edges that allow for sufficient material flow to form a bond, the punches located in the central section are highly restricted. This localized flow restriction at the center is coupled with the maximum elastic tool deflection, which naturally occurs at the mid-span of the tooling setup, under the massive 470 kN load. This combination of maximum tool deflection at the die center and severe inter-punch flow interference effectively reduced the local energy density below the threshold required for solid-state bonding. This comprehensively explains why the eight-punch specimen achieved forge joining at the ends but experienced a weak bond and subsequent separation in the central area.

While a hat-bending die was used, joining was successfully achieved through forge joining. However, further improvements are needed. Based on the experimental results, increasing the nominal compression ratio by making the punches protrude further from the lower die to compensate for deflection should be observed. In addition, positioning the punches so that their centers align with the edges of the specimen would likely facilitate the material flow, leading to an even greater increase in the actual compression ratio. Other potential improvements include optimizing the number of punches or changing their shape to effectively raise the local compression ratio. Therefore, further research is necessary to establish more robust conditions for achieving forge joining during hat bending. Finally, the measurement difficulties associated with shear tensile tests on hat-bending specimens mean that establishing a specialized testing methodology is a crucial future consideration.

6. Conclusions

The forge joining of Al-Si-coated 22MnB5 steel sheets was conducted using various punch shapes, and the joint strength was evaluated. In addition, finite element simulations were performed during the joining process to investigate the effects of the contact pressure and surface expansion rate on the joint strength. As a result, the following findings were obtained.

(1) When comparing punches with the same projected area but different geometric features, the cross-shaped punch exhibited the highest joint strength, improving the joint strength by approximately 80% compared to a circular punch. The maximum tensile shear load showed a strong positive correlation with both the total perimeter of the punch tip and the punch perimeter at the upper sheet contact area.

(2) Using a 2:1 rectangular punch improved the tensile shear load of the joint, increasing the joint strength by about 60% compared to a 1:1 square punch. Among rectangular punches with different aspect ratios, the tensile shear load also showed a strong positive correlation with the punch perimeter on the upper sheet side. However, it did not show a strong correlation with the total perimeter of the punch tip.

(3) Adding a slope to the tip of a rectangular punch increased the deformation of the upper sheet at the joint, but the joint strength either decreased or remained unchanged. No change in joint strength was observed, due to the direction of the slope. Investigation into the influence of the inclination direction on the joint strength revealed no significant differences; the average joint strength values consistently ranged from 0.7 to 1.3 kN. Therefore, a substantial enhancement in joint strength is not anticipated through alterations in the inclination's orientation.

(4) A certain degree of contact pressure and surface expansion rate is necessary for joining. When comparing punches with the same projected area, punch shapes that had a relatively uniform distribution of contact pressure and surface expansion rate, rather than a uniform distribution, tended to show higher joint strength. This trend was particularly evident and was consistently observed for contact pressure across all conditions.

(5) Forge joining using a hat-bending die was confirmed. The actual compression rate of the punch is lower than the flat die set to the same nominal compression ratio, and it is necessary to improve the compression ratio.

Author Contributions: Conceptualization, J.C. and T.M.; methodology, J.C., T.M. and T.I.; software, T.I. and T.M.; validation, J.C., T.M. and T.I.; formal analysis, J.C., T.M. and T.I.; investigation, J.C., T.M. and S.S.; resources, T.M.; data curation, J.C., T.M. and T.I.; writing—original draft preparation, J.C. and T.I.; writing—review and editing, J.C., T.M. and S.S.; visualization, J.C. and T.I.; supervision, T.M. and S.S.; project administration, T.M.; funding acquisition, J.C. and T.M. All authors have read and agreed to the published version of the manuscript.

Funding: This research was supported by the Petchra Pra Jom Klao Ph.D. Research Scholarship from King Mongkut's University of Technology Thonburi.

Data Availability Statement: The original contributions presented in this study are included in the articlel. Further inquiries can be directed to the corresponding author.

Acknowledgments: The authors gratefully acknowledge the invaluable support of Masahito Ouchi and Kazuki Yamamoto for the experiments and data analysis. The authors express their gratitude for the financial support received through the Petchra Pra Jom Klao Ph.D. Research Scholarship from King Mongkut's University of Technology Thonburi.

Conflicts of Interest: The authors declare no conflicts of interest.

References

1. Fan, J.; Meng, X.; Tian, J.; Xing, C.; Wang, C.; Wood, J. A review of transportation carbon emissions research using bibliometric analyses. *J. Traffic Transp. Eng. (Engl. Ed.)* **2023**, *10*, 878–899. [CrossRef]
2. Zhang, W.; Xu, J. Advanced lightweight materials for Automobiles: A review. *Mater. Des.* **2022**, *221*, 110994. [CrossRef]
3. Tisza, M.; Czinege, I. Comparative study of the application of steels and aluminium in lightweight production of automotive parts. *Int. J. Lightweight Mater. Manuf.* **2018**, *1*, 229–238. [CrossRef]
4. Sandrini, G.; Chindamo, D.; Gadola, M.; Candela, A.; Magri, P. Exploring the Impact of Vehicle Lightweighting in Terms of Energy Consumption: Analysis and Simulation on Real Driving Cycle. *Energies* **2024**, *17*, 6398. [CrossRef]
5. Votava, F.; Jirková, H.; Kučerová, L.; Jeníček, Š. Study of Transition Areas in Press-Hardened Steels in a Combined Tool for Hot and Cold Forming. *Materials* **2023**, *16*, 442. [CrossRef]
6. Li, J.; Tong, C.; Zhang, R.; Shi, Z.; Lin, J. A data-informed review of scientific and technological developments and future trends in hot stamping. *Int. J. Lightweight Mater. Manuf.* **2024**, *7*, 327–343. [CrossRef]
7. Li, X.; Chang, Y.; Wang, C.; Hu, P.; Dong, H. Comparison of the hot-stamped boron-alloyed steel and the warm-stamped medium-Mn steel on microstructure and mechanical properties. *Mater. Sci. Eng. A* **2017**, *679*, 240–248. [CrossRef]
8. Hou, Z.; Liu, Y.; He, Q.; Wang, J.; Min, J. Low-Carbon-Emission Hot Stamping: A Review from the Perspectives of Steel Grade, Heating Process, and Part Design. *Automot. Innov.* **2023**, *6*, 324–339. [CrossRef]
9. Mori, K.; Bariani, P.; Behrens, B.-A.; Brosius, A.; Bruschi, S.; Maeno, T.; Merklein, M.; Yanagimoto, J. Hot stamping of ultra-high strength steel parts. *CIRP Ann.* **2017**, *66*, 755–777. [CrossRef]
10. Li, Z.; Wang, L.; Wang, Z.; Wang, J.; Xu, W. A Comprehensive Review towards Oxidation Resistant Press-Hardened Steels. *High-Temp. Mater.* **2025**, *2*, 10004. [CrossRef]
11. Nakagawa, Y.; Mori, K.-I.; Maeno, T. Springback-free mechanism in hot stamping of ultra-high-strength steel parts and deformation behaviour and quenchability for thin sheet. *Int. J. Adv. Manuf. Technol.* **2017**, *95*, 459–467. [CrossRef]
12. Merklein, M.; Johannes, M.; Lechner, M.; Kuppert, A. A review on tailored blanks—Production, applications and evaluation. *J. Mater. Process. Technol.* **2014**, *214*, 151–164. [CrossRef]
13. Wang, X.; Wang, S.; Lu, R.; Xuan, Y.; Zhang, S.; Zhang, G.; Hu, X.; Liu, X.; Chen, L. Research Progresses on Technologies and Theory of Blanks with Variable Thicknesses. *Materials* **2024**, *17*, 4450. [CrossRef]
14. Lei, C.; Xing, Z.; Xu, W.; Hong, Z.; Shan, D. Hot stamping of patchwork blanks: Modelling and experimental investigation. *Int. J. Adv. Manuf. Technol.* **2017**, *92*, 2609–2617. [CrossRef]
15. Merklein, M.; Wieland, M.; Lechner, M.; Bruschi, S.; Ghiotti, A. Hot stamping of boron steel sheets with tailored properties: A review. *J. Mater. Process. Technol.* **2016**, *228*, 11–24. [CrossRef]
16. Li, W.; Zhang, Z.; Jia, H.; Ren, M. The Optimization of Welding Spots' Arrangement in A-Pillar Patchwork Blank Hot Stamping. *Metals* **2023**, *13*, 1409. [CrossRef]
17. Lara, J.A.C.; Abbade, L.; Mucsi, C.S.; Nizes, A.D.C.; Rossi, J.L. Study of Patchwelded Blanks Resistance Spot Welding (RSW) Before Hot Stamping with and without Heat Treatment Parameters. *Mater. Res.* **2023**, *26*, e20230053. [CrossRef]
18. Zhang, Z.; Ouyang, X.; Zhu, L. Study on the hot stamping simulation and experiment of A-pillar patchwork blanks. *Int. J. Adv. Manuf. Technol.* **2022**, *122*, 365–376. [CrossRef]
19. Mori, K.-i.; Kaido, T.; Suzuki, Y.; Nakagawa, Y.; Abe, Y. Combined process of hot stamping and mechanical joining for producing ultra-high strength steel patchwork components. *J. Manuf. Process.* **2020**, *59*, 444–455. [CrossRef]
20. Shi, D.; Watanabe, K.; Naito, J.; Funada, K.; Yasui, K. Design optimization and application of hot-stamped B pillar with local patchwork blanks. *Thin-Walled Struct.* **2022**, *170*, 108523. [CrossRef]
21. Mori, K.-i.; Bay, N.; Fratini, L.; Micari, F.; Tekkaya, A.E. Joining by plastic deformation. *CIRP Ann.* **2013**, *62*, 673–694. [CrossRef]
22. Meschut, G.; Merklein, M.; Brosius, A.; Drummer, D.; Fratini, L.; Füssel, U.; Gude, M.; Homberg, W.; Martins, P.; Bobbert, M.; et al. Review on mechanical joining by plastic deformation. *J. Adv. Join. Process.* **2022**, *5*, 100113. [CrossRef]
23. Lu, Y.; He, Q.; Chen, Y.; Wang, Y.; Chen, C. A review on the strengthening methods to improve mechanical properties of clinched joints. *Int. J. Adv. Manuf. Technol.* **2025**, *137*, 4435–4469. [CrossRef]
24. Qiu, P.; Lu, X.; Dai, X.; Deng, B.; Xiao, H. Center-Punching Mechanical Clinching Process for Aluminum Alloy and Ultra-High-Strength Steel Sheets. *Metals* **2024**, *14*, 1190. [CrossRef]
25. Fu, L.; Zhang, S.; Qiu, P.; Xiao, H.; Deng, B.; Lu, X. Optimization of Clinching Joint Process with Preforming between Ultra-High-Strength Steel and Aluminum Alloy Sheets. *Metals* **2024**, *14*, 767. [CrossRef]
26. Chen, L.-W.; Cai, M.-J. Development of a hot stamping clinching tool. *J. Manuf. Process.* **2018**, *34*, 650–658. [CrossRef]
27. Abe, Y.; Tatara, Y.; Hosokawa, T.; Yamauchi, R. Clinch-Bonding Process for Ultra-High-Strength Steel and A5052 Aluminum Alloy Sheets. *Materials* **2025**, *18*, 3556. [CrossRef]
28. Chen, H.; Zhu, Z.; Zhu, Y.; Sun, L.; Guo, Y. Solid-State Welding of Aluminum to Magnesium Alloys: A Review. *Metals* **2023**, *13*, 1410. [CrossRef]

29. Yamagishi, H. Cu/Al Dissimilar Cold Spot Forge Welding: Effects of Bonding Temperature and Reduction Ratio on Joint Strength and Reaction Layer Growth. *Metall. Mater. Trans. A* **2023**, *54*, 3519–3536. [CrossRef]
30. Yamagishi, H.; Hisada, Y.; Otsubo, T.; Omori, N. Multilayer bonding of A1N30H foils to A1050 plates using cold spot forge welding. *Heliyon* **2023**, *9*, e23103. [CrossRef] [PubMed]
31. Japanese Standards Association. *Ferrous Materials & Metallurgy Handbook*; Japanese Industrial Standards Committee: Tokyo. Japan, 2023.
32. Japanese Standards Association. *Specimen Dimensions and Procedure for Shear Testing Resistance Spot and Embossed Projection Welded Joints*; Japanese Industrial Standards Committee: Tokyo, Japan, 1999.
33. Oberpriller, B.; Burkhardt, L.; Griesbach, B. Benchmark 3 Continuous Press Hardening. In Proceedings of the 7th International Conference and Workshop on Numerical Simulation of 3D Sheet Metal Forming Processes (Numisheet 2008), Interlaken, Switzerland, 1–5 September 2008; pp. 115–129.
34. Hexagon. *Simufact Forming 2023.3 Application Manual*; Simufact Engineering GmbH: Hamburg, Germany, 2023.
35. Hexagon. *Marc 2024.2 Volume A: Theory and User Information*; Hexagon Manufacturing Intelligence: Surrey, UK, 2024.

Disclaimer/Publisher's Note: The statements, opinions and data contained in all publications are solely those of the individual author(s) and contributor(s) and not of MDPI and/or the editor(s). MDPI and/or the editor(s) disclaim responsibility for any injury to people or property resulting from any ideas, methods, instructions or products referred to in the content.